Water column poly-aromatic hydrocarbon anomalies measured with submersible gliders in the Angolan natural oil seepage province

Romain Jatiault, Damien Dhont, Florent Besson, Marc Tedetti, Orens Pasqueron de Fommervault, Lies Loncke, François Bourrin, Madeleine Goutx, Xavier Durrieu de Madron

Water column poly-aromatic hydrocarbon anomalies measured with submersible gliders in the Angolan natural oil seepage province

Romain Jatiault[1*], Damien Dhont[2], Florent Besson[3], Marc Tedetti[4], Orens Pasqueron de Fommervault[3], Lies Loncke[1], François Bourrin[1], Madeleine Goutx[4], Xavier Durrieu de Madron[1]

[1] Centre de Formation et de Recherche sur les Environnements Méditerranéens (CEFREM), UMR 5110, 52 Avenue Paul Alduy, 66100 Perpignan, France.
[2] Total SA, Centre Scientifique et Technique Jean Feger (CSTJF), Avenue Larribau, 64018 Pau, France.
[3] Alseamar (ALCEN), 60 Avenue Olivier Perroy, 13790 Rousset.
[4] Aix-Marseille Univ., Université de Toulon, CNRS, IRD, Mediterranean Institute of Oceanography (MIO), UMR110, 13288 Marseille, France.
Correspondence to : Romain Jatiault (romain.jatiault@univ-perp.fr), Centre de Formation et de Recherche sur les Environnements Méditerranéens (CEFREM), UMR 5110, 52 Avenue Paul Alduy, 66100 Perpignan, France.

Key Points:

- We combined satellites and an underwater glider to monitor natural hydrocarbon seepage in the Lower Congo basin.
- The detection performance of an underwater glider is evaluated for the detection of natural oil seeps.
- Hydrocarbon presence in the water column is well expressed in the pyrene channel as vertical high-amplitude signals.
- Fluorescence measurements suggest a trapped plume of hydrocarbon in the oxygen minimum zone.

Keywords: Glider, Fluorescence, Polycyclic aromatic hydrocarbons, Seeps, Oxygen Minimum Zone.

Abstract.

Fluorescence sensors mounted on unmanned underwater gliders open new ways of investigation to detect dissolved hydrocarbons in seawater. A glider was deployed for 20 days to monitor biogeochemical and physical signals associated with natural hydrocarbon seepages within the first 700 m in the Angolan waters. The glider was equipped with fluorometers (MiniFluo-UV) to measure the concentrations of polycyclic aromatic hydrocarbons (PAH) of interest, i.e. naphthalene, phenanthrene, fluorene and pyrene. A continuous PAH-like signal detected within the 70 m layer below the sea surface is associated with high chlorophyll concentration in the deep chlorophyll maximum. Vertical PAH-like anomalies forming either strong spikes or diffuse columns down to 700 m are observed at the exact location of oil seep sites identified on Synthetic Aperture Radar satellite images. An ~200 m thick layer of enhanced PAH-like concentration, topped by a thermo/pycnocline identified at 280-300 m water depth, is measured in concomitance with the decrease in oxygen concentration. The concomitance of these signals suggests that lower oxygen concentrations induce a preservation of hydrocarbons within the eastern Atlantic oxygen minimum zone. Even if the absence of in-situ measurements limits the understanding of physical and biogeochemical processes affecting PAH concentrations, the measurements conducted at the edges of the OMZ suggests a relationship with microbial activity and organic matter dynamics in this layer. The results presented here show that gliders equipped with PAH sensors represent a promising means for monitoring hydrocarbons in the oceans, especially when they are coupled with other systems (i.e. Synthetic Aperture Radar).

1. Introduction

The volume of hydrocarbons expelled in the marine environment from natural processes (Wilson et al., 1973) is estimated to be equivalent to man-made pollutions (c.f. Deep-Water Horizon, Gulf of Mexico; Prince et al., 2003). Among the different compounds, the polycyclic aromatic hydrocarbons (PAH) in the ocean are mainly sourced from the atmosphere with a monthly amount of four times the total volume released from the Deep-Water Horizon blowout (González-Gaya et al., 2016), which suggests that natural hydrocarbon seepage represents only about 2% of this volume. In the case of natural seepage, hydrocarbons are released from the seafloor as bubbles of oil and/or gas in the water column (Macdonald et al., 2002; Greinert et al., 2006; McGinnis et al., 2006; Korotenko et al., 2016; Jatiault et al., 2018a). Synthetic Aperture Radar

(SAR) systems aboard satellites are commonly used to detect oil films at the sea surface (e.g. Bern, 1992; Espedal and Johannessen, 2000; Brekke and Solberg, 2005; Leifer et al., 2012). While the oil seepage mechanism is discontinuous (Garcia-Pineda et al., 2010; Jatiault et al., 2017), the redundancy of seepage slicks on a stack of multi-temporal satellite images enables discrimination with mono-temporal man-made pollutions (MacDonald et al., 2015) and other false positives (i.e. algal bloom; Espedal and Wahl, 1999). Seabed coring and imaging with remotely operated vehicles provide a direct investigation method for seafloor seep activity (Abrams, 2005), while investigation of the hydrocarbons in the water column is limited to bubble-related acoustic anomalies (Greinert et al., 2006; Dupré et al., 2014; Loranger et al., 2018).

Hydrocarbons are composed of three main families, i.e. saturated hydrocarbons (e.g. alkanes), unsaturated hydrocarbons (e.g. alkenes), monocyclic (e.g. benzene) and poly-aromatic hydrocarbons (e.g. PAH) consisting of two or more fused benzene rings. PAH have toxic (carcinogenic and mutagenic) effects on marine organisms and can bio-accumulate in the food chains (Hylland, 2006). Some of them are listed among priority contaminants (European Union, United States FWPCA and EPA; Alexander et al., 2008). Under oil spill conditions, low molecular weight petrogenic compounds, such as naphthalene (Naph), phenanthrene (Phe), fluorene (Flu) and their alkylated derivatives, become preponderant within the accumulation of dissolved PAH in seawater (González et al., 2006; Zhou et al., 2013).

While most of the released hydrocarbons reach the surface and are detectable with space-borne sensors (Fingas and Brown, 2014; Jatiault et al., 2017), a consistent volume potentially remain stored in intermediate waters (Camilli et al., 2010; Adalsteinsson et al., 2011; Wade et al., 2011; Camassa et al., 2013; Landeau et al., 2014). Among the variety of autonomous underwater platforms that are used for submarine applications (e.g. Nicholson and Healey, 2008), buoyancy-driven underwater gliders are particularly useful for understanding hydrocarbon patterns in the water column (e.g., Wood, 2009; Testor et al., 2010; Jenkins and D'Spain, 2016, Dhont et al., 2019). Indeed, underwater gliders or 'gliders' are characterized by low energy consumption, which permits multiple weeks of autonomy without any human intervention and therefore long-term observations without reconditioning (Rudnik and Zerres, 2004; Meyer, 2016).

Numerous and varied sensors can be mounted on the glider platform to measure physical and biogeochemical parameters of the oceans, such as dissolved oxygen, chlorophyll-*a*/pigments, turbidity and dissolved organic matter (Mortier et al., 2012, GROOM report, 2014). PAH are highly fluorescent in the ultraviolet (UV) /blue spectral domains owing to their aromatic

structure (Dabestani and Ivanov, 1999; Ferretto et al., 2014) whereas light absorption by water increases with wavelength (Clarke and James, 19[3]9; Buiteveld et al., 1994; Pope and Fry, 1997; Wozniak and Dera, 2007). Hence, several submersible fluorometers have been proposed in recent years for the in-situ detection of PAH in seawater in the UV domain (Zielinski et al., 2009, 2018; Tedetti et al., 2010; Conmy et al., 2014; Ferdinand et al., 2017). Recently, MiniFluo-UV fluorometers were installed on a glider to monitor polyaromatic hydrocarbons in marine waters (Cyr et al., 2017, 2019). The combination of gliders and submersible fluorometers therefore opens new fields of investigation to monitor the leakage of hydrocarbons, as already performed during the Deep-Water Horizon event (Camilli et al., 2010).

In this study, we report on the first deployment of a glider equipped with dedicated hydrocarbon fluorometers (MiniFluo-UV) to evaluate the effectiveness of PAH sensors mounted on unmanned platforms to assess the fate of naturally expelled hydrocarbons in the water column. The fluorescence signals of dissolved natural hydrocarbon seeps in the ocean will be compared with seepage slicks observed at the sea surface from SAR satellite data acquired simultaneously. The chosen area of study is the Lower Congo Basin, offshore Angola, which is recognized as a prolific oil seepage site in the Atlantic Ocean. These combined observations will be used to discuss the benefits and limitations of hydrocarbon detection using fluorescence sensors on board gliders.

2. The Lower Congo Basin: Regional setting

2.1. Petroleum systems and hydrocarbon seepage manifestations

The deep-water province of the Lower Congo Basin is one of the most active areas in the world regarding the manifestation of natural oil seepage (Jatiault et al., 2017). The oil source rocks correspond to the Early Cretaceous (145 – 125 Ma) Bucomazi Fm (5 to 20% TOC; Burwood, 1999; Schoellkopf and Patterson, 2000) and Late Cretaceous (99 - 65 Ma) Iabe Fm (~10 % TOC; Burwood, 1999; Cole, 2000). The Paleogene (65 - 45 Ma) Landana Fm shows high potential (~4% TOC) but remains thermally immature for hydrocarbon generation (Cole et al., 2000, Schoelköpf and Patterson, 2000). In the Lower Congo Basin, gravitational deformation associated with salt tectonics inhibits the cap rock efficiency of Tertiary series by deforming the overburden, which eases the dismigration of hydrocarbons towards the seafloor (Marton et al., 2000, 2004; Hudec and Jackson, 2004; Guiraud et al., 2010).

Seafloor circular depressions referred to as pockmarks correspond to expulsion sites of hydrocarbons generated in the deeper Cretaceous series (Gay et al., 2007; Andresen et al., 2010; Andresen and Huuse, 2011; Jones et al., 2014, Jatiault et al., 2019a, b). Ultimately, hydrocarbons migrate in the water column before reaching the sea surface (William and Lawrence, 2002; Jatiault et al., 2017, 2018). In the Lower Congo Basin, more than a hundred active oil seep sites have been detected using multi-temporal series of satellite SAR images, for water depths ranging from 1000 to 3000 m (Jatiault et al., 2017; Fig. 1a).

2.2. Hydrographic conditions

2.2.1. Water masses

The surficial water masses of the Lower Congo Basin are strongly influenced by the Congo River, the world's second largest river in terms of the discharge volume of water (average 41 200 m^3/s; Ukwe et al., 2006; Dupont, 2013). The Congo Plume brings fresh water to the basin at a shallow depth (0-10 m; Hopkins et al., 2013; estuary at 6°S, to the north of the map in Fig. 1a). Multiple currents are reported in the Lower Congo Basin depending on the water depth (Fig. 1a). In the 0-300 m layer, the main reported current is the Angolan current, which transports equatorial waters towards the south (Moroshkin et al., 1970; Hardman-Mountford et al., 2003), even if the seasonal intrusions of the northward Benguela current modifies the displacement of water masses in the area (Jatiault et al., 2018). The Angolan current is steady, narrow and fast (20 to 50 cm/s), with water temperatures greater than 24 °C and with a salinity of more than 36.4 in the upper mixed layer (Lass et al., 2000). The 300-500 m layer corresponds to a transition to deeper water masses and no prominent current is reported in the literature. The intermediate water circulation (500-1000 m) is controlled by the southward-flowing Southern Intermediate Counter Current, transporting the South Atlantic Central Water (Stramma and England, 1999; Stramma and Scott, 1999; Shannon, 2001). The Angolan gyre is a retroflection loop centred further south of our study area (10°S, 8°E) that seasonally impacts the circulation of surface, sub-surface and intermediate water masses (Mazeika, 1967; Moroshkin et al., 1970; Peterson and Stramma, 1999; Doi et al., 2007). Deep-water circulation along the Angolan coast is influenced by the North Atlantic Deep Water flowing slowly (~2cm/s; Lynn, 1971) to the south at 2000 m depth (Stramma and England, 1999; Arhan et al., 2003). It also corresponds to the eastern retroflection of the Deep Western Boundary Current (Garzoli et al., 2015).

2.2.2. Oxygen Minimum Zone

The study area lies in the South Atlantic Oxygen Minimum Zone (OMZ) in relation with the Northern Benguela Upwelling System (Schmidt and Eggert, 2016). OMZs are defined as volumes of interior oceans characterized by low Dissolved Oxygen (DO) concentration. A restrictive threshold value of 45 µmol/kg is commonly considered, even though a more relaxed DO concentration of 90 µmol/kg has also been reported (Karstensen et al., 2008). OMZs are mostly distributed at the eastern edges of tropical oceans for water depths ranging from 100 to 900 m (Karstensen et al., 2008). The threshold of 45 µmol/kg is located between 300 and 500 m in the South Atlantic (Mercier et al., 2003; Karstensen et al., 2008; Mashifane et al., 2016; Schmidt and Eggert, 2016), while a suboxic water layer (DO < 90 µmol/kg) is reported to be 600 m thick (Mercier et al., 2003; Karstensen et al., 2008; Schmidt and Eggert, 2016). Oceanic gyres correspond to hydrologic isolation areas. The presence of the Angolan gyre in the area significantly modifies the spatiotemporal distribution of DO in the Angolan OMZ (Teuber et al., 2013) and, indirectly, the biological processes (Stramma et al., 2012; Wright et al., 2012; Schmidt and Eggert, 2016).

2.2.3. Oceanic conditions during the glider mission

Maps of geostrophic currents were produced to assess large and mesoscale circulation over the studied area. The water velocity was derived from sea level altimeter anomalies using satellite products (Jason-3, Sentinel-3A, HY-2A, Saral/AltiKa, Cryosat-2, Jason-2, Jason-1, T/P, ENVISAT, GFO, ERS1/2) with daily temporal resolution and 0.25 × 0.25 degree spatial resolution (http://duacs.cls.fr).

The mission lasted 20 days from the deployment of the glider on 29 October to its recovery on 18 November 2017. We extracted geostrophic surface currents (the balance between the pressure gradient force and the Coriolis force) from altimeter satellite measurements (Fig. 1b). The main large-scale geostrophic currents identified during the mission are (i) a strong coastal surface current (30-40 cm/s) that flowed to the east at the beginning of the mission and turned progressively northwards at its end (Fig. 1b), and (ii) the clockwise Angolan gyre loop located in the south (centred on 8.5°S, 10.5°E). At the beginning of the mission, the northern edge of the Angolan gyre impacted the southern limit of the study area. The Congo Plume is not observed on the sea surface currents maps. To sum up, the glider remained isolated from large-scale hydro-dynamic structures during the mission (Fig. 1b) with surface currents lower than 0.10 m/s.

3. Data and methods

3.1. Satellite data

During the mission, natural oil seepages were monitored with the acquisition of 49 satellite Synthetic Aperture Radar (SAR) scenes combining free-access Sentinel-1 (ESA) and commercial Radarsat, Cosmo-Skymed and TerraSAR-X data (**Fig. 2**a, b). The temporal distribution of SAR data is homogeneous, with generally one image every 12 hours. Oil slicks at the sea surface were detected with the SAR system because of the contrast in roughness with free water (e.g. Alpers and Espedal, 2004).

3.2. Glider data

3.2.1. Acquisition strategy

The navigation mode of underwater gliders is driven by buoyancy changes controlled by the successive inflation/deflation of an external bladder (Davis et al., 2002). This results in alternating upward and downward movements that create a synergistic forward movement along V-shaped acquisition profiles commonly called 'yos'. The glider can rely on its rudder at the rear of the hull to keep to the planned trajectory despite possible drifting due to the ocean currents.

During the mission, the SeaExplorer glider was limited to a investigation depth of 700 m. The GPS position of the glider was remotely monitored by Iridium satellite and the data collected by the sensors were transmitted in near-real time at each surfacing. The underwater currents were estimated from the horizontal distance between the measured versus expected surfacing area of the glider (Kim et al., 2014). Estimated underwater positions or dead reckoning can be derived from navigation data including the pitch (α), heading, depth and vertical speed (Davis et al., 2002). The acquisition frequency is 20 s for navigation data and 5 s for sensor measurements.

The strategy employed for piloting the glider included parallel transects and virtual moorings (**Fig. 2**b). Virtual moorings consist in a succession of yos at different depths (typically between 100 and 700 m) centred on the location of oil seep sites with a progressive variation of the orientation of profile direction. This navigation style results in rosette patterns with a radius of a few kilometres.

Large transects with a maximum depth amplitude (700 m) were carried out to connect the different seep sites investigated during the mission. The glider survey was designed to target the largest number of active hydrocarbon seepage areas (**Fig.**

171 **2**c). Acquisition phase 1 of the mission was planned to fly above three oil seep sites numbered 1, 2 and 3 (**Fig. 2**c) and
172 characterized by a high percentage of seepage slick occurrence (Jatiault et al., 2017). The strategy adopted during the second
173 phase of acquisition was to follow a pseudo-regular grid consisting in ~50 km profiles along the west-east direction for the
174 investigation of seep sites of lower frequency emission (seeps 4 to 7). To enhance the visualization of the data collected, the
175 section displayed in this paper gathers the data along a 1.5 km wide strip that follows the acquisition direction of the glider
176 (see section distance markers in **Fig. 2**b). The distance between measurement points is typically one metre; an interpolation
177 was used to link discrete measurements in order to produce two-dimensional isocontour maps.

178 ***3.2.2. Sensors and data processing***

179 **PAH detection using the MiniFluo-UV sensors**

180 A miniaturized (MiniFluo-UV) fluorometer sensor was mounted on the glider for in-situ measurements of polyaromatic
181 hydrocarbons (PAH) and dissolved organic matter descriptors (Tedetti et al., 2013; Cyr et al., 2017, 2019). The MiniFluo-
182 UV has two optical channels, enabling the simultaneous detection of two fluorescent compounds (fluorophores) of interest
183 according to their excitation/emission wavelength ($\lambda_{Ex}/\lambda_{Em}$) couple. Overlaps may occur between the fluorescence of
184 dissolved PAH and that of protein- and humic-like compounds of marine organic matter (Nieke et al., 1997; Parlanti, 2000;
185 Para et al., 2010; Conmy et al., 2014; Zhao et al., 2017). Therefore, the MiniFluo-UV highlights fluorescence signatures
186 having a high probability of being PAHs (PAH-like). The petroleum origin of PAH-like is estimated by comparing the
187 distribution patterns of PAH-like fluorophores with the distribution patterns of physical and biogeochemical parameters of
188 the investigated environment. The more the properties of the 4 PAH-like fluorophores are decoupled from those of
189 chlorophyll-a and humic-like, the more likely it is that they correspond to PAH responses and not to protein-like
190 fluorophores.
191
192 The sensor can operate in two configurations:
193 1) MiniFluo-UV-1 for the simultaneous detection of phenanthrene-like (Phe-like) and naphthalene- (Naph-like) or
194 tryptophan-like (Trp-like) compounds, with fluorescence measurements at $\lambda_{Ex}/\lambda_{Em}$ of 255/360 nm (Phe-like) and 275/340 nm
195 (Naph-like and Trp-like).

196 2) MiniFluo-UV-2 for the simultaneous detection of fluorene-like (Flu-like) and pyrene-like (Pyr-like) compounds, with
197 fluorescence measurements at $\lambda_{Ex}/\lambda_{Em}$ of 260/315 nm (Flu-like) and 270/380 nm (Pyr-like).
198 While Naph (2-rings), Phe and Flu (3-rings) are low molecular weight PAH of petrogenic origin (i.e. issued from crude
199 oil/petroleum or its derivatives), Pyr (4-rings) is a medium molecular weight PAH of pyrogenic origin (i.e. issued from the
200 combustion of fossil fuels; Alexander et al., 2008). Trp is an aromatic amino acid associated with microbial processes
201 (bacteria and phytoplankton) in marine waters. The exact superimposition between the fluorescence spectral domains of
202 Naph and Trp compounds (Tedetti et al., 2010; Xu et al., 2011) prevent their discrimination based on steady-state
203 fluorescence measurements (Tedetti et al., 2010, 2012; Stedmon and Cory, 2014).
204 The raw fluorescence data of the MiniFluo-UV are provided in electronic counts. We followed the method exposed by Cyr et
205 al. (2017, 2019) to normalize and convert the fluorescence electronic counts into fluorophore mass concentrations (g/L) by
206 using appropriate calibration parameters. As recommended by Cyr et al. (2017), the MiniFluo-UV-1 and -2 were calibrated
207 in the laboratory before the cruise using individual PAH (Phe, Naph, Fluo, Pyr), as well as Trp standards (Supelco, Sigma-
208 Aldrich) diluted in ultrapure (Milli-Q) water at final concentrations ranging from 0.1 to 10 µg/L. The limits of detection of
209 each PAH and Trp are reported in Table 1. For all these compounds, the MiniFluo-UV measurement precision was ≤ 2%,
210 meaning that a signal modification > 2% can be considered as indicative of environmental changes.
211 The calibration of the MiniFluo-UV was performed using individual standard (parent) PAH, which assumes that all
212 dissolved PAH present in seawater are in the non-alkylated form. As alkylated homologues generally have the same
213 fluorescence maxima positions as their parent compounds (Nijegorodov et al., 2009; Ferretto et al., 2014), the MiniFluo-UV
214 sensors actually record the fluorescence signals of alkylated and non-alkylated Naph, Phe, Flu and Pyr, albeit they are not
215 taken into consideration in the calibration procedure. This may lead to overestimations of true PAH concentrations in marine
216 waters (Cyr et al., 2019). Fluorescence quenching refers to any process that decreases the fluorescence intensity of a
217 fluorophore through molecular interactions with a quencher molecule. In seawater, the fluorescence intensity of PAH-like
218 fluorophores may be quenched (reduced) by interactions with oxygen (collisional/dynamic quenching at excited state) or
219 dissolved organic matter (contact/static quenching, i.e., formation of a non-fluorescent complex at the ground state), leading
220 to potential underestimation of the real concentrations of these fluorophores (Cullen and Lewis, 1995; Gauthier et al., 1996).

Although PAH-like measurements provide estimated values of PAH-like concentrations, the coherency of PAH patterns observed in the water column validates the detection of anomalous signals by the sensor.

Other sensors

Conductivity Temperature Depth sensor

The Glider Pumped Conductivity Temperature Depth sensor developed by Seabird provides physical measurements of the seawater such as Potential Temperature (θ), Practical Salinity (Sp), Absolute Pressure (P) and Potential Density Anomaly (σ_θ) according to conversion equations in the TEOS-10 manual (IOC et al., 2010). The practical salinity was derived from raw conductivity and absolute pressure measurements and the potential density anomaly was derived from potential temperature, practical salinity and absolute pressure. The resolution of the sensor is 10^{-5} S/m for Conductivity, 0.001 °C for temperature and 0.002 for pressure.

Oxygen sensor

The glider was also equipped with an oxygen sensor (SBE-43F) to measure concentrations of dissolved oxygen (DO; µmol/kg). Computation of oxygen concentrations in physical units was performed according to the Seabird SBE43 recommendations (Owens and Millard, 1985) and by using calibration coefficients specific to the sensor. The initial accuracy is 2% of concentration.

FLBBCD sensor

The Wetlabs ECO fluorometer and backscattering (FLBBCD) sensor provides fluorescence measurements of chlorophyll-*a* and dissolved humic substances (humic-like) together with the raw backscattering signal at 700 nm (BB700) used for particle concentration and turbidity (Table 1). Following manufacturer recommendations (Dall'Olmo et al., 2009), raw counts of the sensor were converted into concentrations of fluorophores expressed in mg/m^3 for chlorophyll-*a* and in Quinine Sulphate Units (1 QSU = fluorescence of 1 µg/L of quinine sulphate) for humic-like concentrations. The raw backscattering value for BB700 is expressed in 1/m.sr (volume scattering function at a centroid angle of 140°), from which we derived the particulate backscattering (b_{bp700}) that is a proxy of the particulate organic carbon concentration in the open sea (Stramski and Morel, 1990). The instrument resolution is 1.3 counts.

4. Results

4.1. Sea surface manifestations of hydrocarbon seeps during the glider mission

The analysis of the 49 available Synthetic Aperture Radar (SAR) scenes (see the temporal distribution in **Fig. 3**) identified a total of 675 slicks during the 20 days of the glider survey, thus confirming the high activity of oil leakages at the location of natural oil seep sites (**Fig. 3**a). Oil slicks were mostly deflected towards the northeast in the southern portion of the survey area and towards the north in the northern area (**Fig. 2** and **Fig. 3**a). A large majority of oil seep sites identified between 1994 and 2016 (Jatiault et al., 2017) were active during the glider mission, whereas some others remained dormant. The 7 seep sites investigated were intermittent with a percentage of slick occurrence varying from 7% to 70%.

4.2. Water masses

Underwater currents were estimated from the glider position and averaged through the 0-700 m layer. Currents flowed westward during phase 1 and north-westward during phase 2 with relative velocities of 20 to 30 cm/s (**Fig. 4**a).

The conductivity-temperature-depth sensor showed distinct water masses that remained consistent throughout the glider survey. A homogeneous shallow (first 25 m) buoyant water mass characterized by a high temperature (27°C), low salinity (35.2), low density (~23 kg/m^3) and high dissolved oxygen (DO) values (~200 µmol/kg) was present throughout the mission (**Fig. 4**b, c). Between 25 and 50 m, a transition zone is marked by strong gradients of temperature (from 27 to 21 °C), salinity (35.2 to 36) and density (23 to 25.5 kg/m^3) that can be compared to a thermocline or seasonal pycnocline. Maximum salinity values of *Sp* (36.5) occurred at the base of this pycnocline. Between 50 to 280 m, a homogeneous subsurface layer was identified with a classic depth-dependent decrease in θ (from 18 to 13 °C), *Sp* (35.3-36) and σ_θ (26-26.5 kg/m^3). The DO progressively decreases to reach suboxic levels (DO < 90 µmol/kg) at ~150 m. Between 280 and 300 m, a second high thermal gradient develops but is less pronounced than the thermocline. It is observed in association with a decrease in *Sp* (35.3 to ~35) and an increase in θ (15 to 12°C), thus generating a higher σ_θ contrast (**Fig. 4**d). This second pycnocline, namely the permanent pycnocline, marks the transition towards a depleted DO layer (**Fig. 4**e). Concentrations of DO reach suboxic values (DO from 45 to 60 µmol/kg) consistent with that of the oxygen minimum zone (OMZ) for water depths

ranging between 280 to 350 m in the southern area and between 280 to 500 m in the north. DO concentrations in the core of the OMZ drop to ~30 µmol/kg, giving incoherent values because they are below the detection threshold of the sensor. Below the depleted DO layer, concentrations progressively increase up to 100 µmol/kg at 700 m depth, while θ, *Sp and* σ_θ vary linearly with the water depth.

To sum up, the water column remained rather well stratified during the glider survey, yet a relatively strong density gradient is observed at ~280 m (**Fig. 4**d). Isopycnal levels are slightly shifted upwards starting from the 60 km mark on the section distance. This area is also characterized by a thickness variation of the OMZ from roughly 150 m in the south to 50 m in the north.

4.3. Biogeochemical parameters

High concentrations of chlorophyll-*a*-like occur below the fresh water layer for depths between 20 and 60 m with a fluorescence maximum of 6 mg/m^3 at ~50 m (**Fig. 5**a). The minimum chlorophyll-*a* -like concentrations are situated right below the photic zone at 60 m. To a more moderate extent, a slight increase in concentration is observed in the ~300-500 m depth range corresponding to the OMZ and suboxic layers.

Humic-like concentrations are relatively high, generally greater than 0.8 QSU, with a progressive increase in the values along the section distance (**Fig. 5**b). There is a good correspondence between maximal humic-like and chlorophyll-*a* -like concentrations, particularly along the seasonal thermocline (~1.60 QSU). The OMZ layer (350-400 m) also emphasizes a slight increase in humic-like values (~1.30 QSU), especially in the northern area (~50 km north of the seep 1, **Fig. 2**c).

As for humic-like records, the total particle concentration (b_{bp700}) progressively increases with time. High concentrations in b_{bp700} are observed in the first 100 m (0.0004/m.sr), which is followed by a strong decrease with depth (**Fig. 5**c). Patches of relatively higher b_{bp700} values (twice the background) also appear in suboxic and anoxic water layers (0.0007/m.sr; **Fig. 5**c).

4.4. PAH-like fluorophores

Four polyaromatic hydrocarbon (PAH-like) concentrations (Phe-, Naph-, Flu- and Pyr-like) were measured with the two MiniFluo-UV sensors (**Fig. 5**). Background concentrations were close to 0 for the Phe-like channel, ranged from 0.01 to 0.02

293 µg/L for the Flu-like channel, varied from 0.1 to 0.2 µg/L for the Naph-like channel and were greater than 1.4 µg/L for the
294 Pyr-like channel. During the mission, significant increases in concentration occurred on the Pyr- and Flu-like optical
295 channels in comparison to the Phe- and Naph-like channels. A slight decrease of the concentrations of Phe- and Naph-like
296 channels over time should be noted, which can be attributed to a drift of the MiniFluo-UV-1 sensor (**Fig. 6**a, b).

297 ***4.4.1. PAH-like vertical anomalies***

298 PAH-like anomalies in Pyr- and Flu-like optical channels either extend vertically over a few hundred metres or are stratified
299 horizontally in the water column. Vertical anomalies correspond either to spikes, where the PAH-like concentration is
300 several times greater than the regional background for only a few yos, or columnar anomalies, which record a few percent of
301 PAH-like variations during a succession of several yos.

302 Spikes of fluorescence occurred independently from one PAH-like optical channel to another. The Phe-, Pyr- and Flu-like
303 channels display rapid and strong fluctuations of the signal (coloured dots on the vertical profiles of **Fig. 6**a, c, d) while the
304 Naph-like channel does not show anomalous concentrations compared with the background (**Fig. 6**b). The increase in
305 concentration reaches up to 200 times the background for the Pyr-like (< 200 µg/L), 50 times for the Flu-like (1 µg/L) and 3
306 times for the Phe-like (0.4 µg/L) channels. Even though spikes of fluorescence remained occasional throughout the mission,
307 the percentage of spikes recorded by the Pyr-like channel (7.5%) is higher compared with the Flu-like (0.7%) and Phe-like
308 (1%) channels.

309 Vertical spikes of fluorescence are observed on different PAH-like channels from shallow waters down to 500-700 m depths
310 (seep sites 2, 6 and 7). At oil seep site 3, the spikes observed for the Pyr- and Flu-like fluorophores reach only 250 m depth
311 because the glider did not dive deeper at this location. It is worth noting that the spikes mostly occur at the location of oil
312 seep sites observed on satellite images (**Fig. 7**). No specific signal was detected at seep site 5.

313 Four large columnar anomalies are observed in deep layers (350 to 700 m) on the Flu-like channel at distances of 14 to 18,
314 32 to 45, 52 to 56 and 66 to 75 km (**Fig. 6**d) along the section. Each vertical column is delimited upward by the OMZ layer.
315 Flu-like concentrations associated with these anomalies are weak, with only ~3% variation with respect to the regional
316 background. Three out of the four columnar anomalies correspond to the location of oil seep sites as observed on SAR
317 images (1, 2, and 3; **Fig. 7**), while the remaining one is associated with a pockmark on the seafloor (Jatiault et al., 2019b).

318 ***4.4.2. PAH-like horizontal anomalies***

319 We identified two different types of horizontal signals regarding the PAH-like distribution. First, a strong and continuous
320 signal of all the PAH-like channels in the sub-surface water where concentrations of the four PAH-like channels reach their
321 maximum values at ~50-70 m depth (**Fig. 6**). Then, a moderate signal in the intermediate water layers (250 to 450 m) is only
322 detected for the Pyr- and Flu-like channels (**Fig. 6**). This signal is mostly visible through acquisition phase 2 for section
323 distances between the 55 km mark and the end of the mission. The Pyr- and Flu-like responses are rather concordant and
324 show concentration variations of 10% with maximal values at 350 m (1.8 and 0.025 µg/L for the Pyr- and Flu-like channels,
325 respectively). Another moderate PAH-like increase occurs at deeper depths (550-650 m), where the concentration reached
326 1.6 and 0.02 µg/L for the Pyr- and Flu-like channels, respectively. It is worth noting that the b_{bp700} signal is located in the
327 suboxic waters just above and below the Pyr-/Flu-like horizontal plume anomaly (*Fig*. 5c and *Fig*. 6c, d).

328 **5. Discussion**

329 **5.1. Significance of polyaromatic hydrocarbon (PAH-like) concentration anomalies**

330 The MiniFluo-UV measurements showed multiple PAH-like concentration anomalies characterized by:

331 - A consistent strong signal in the subsurface for the four PAH-like channels,
332 - Spike anomalies detected on Flu- and Pyr-like concentrations at the exact location of oil seep sites,
333 - An increase of the Pyr- and Flu-like concentrations within the Oxygen Minimum Zone (OMZ) core (250-450 m) in
334 the northern half of the study area,
335 - Vertical columnar anomalies of the Flu-like channel at the location of oil seep sites.

336 Despite being well visible both on the scattered plots and along the 2D sections, in-situ fluorescence measurements can be
337 influenced by various environmental factors that modify quenching processes (Gauthier et al., 1986; Danielsen et al., 1995;
338 Osburn et al., 2014), among which are temperature (thermal quenching), metal cations and humic substances (static
339 quenching; Danielsen et al., 1995), and molecular oxygen (collisional quenching). Absolute values of PAH-like
340 concentrations reported here shall also be taken with caution since they are directly dependent on the calibration method

employed. Nevertheless, the PAH patterns observed in the water column and the detection of concentration anomalies remain fully relevant.

Two main hypotheses can be envisioned to explain the Flu- and Pyr-like field: (i) protein- and humic-like materials display the same fluorescence signature ($\lambda ex/\lambda em$ couple) couple as PAH and can therefore be misinterpreted as such (PAH look-alike fluorophores; Stedmon et al., 2003), and/or (ii) the effective presence of dissolved hydrocarbons in the water column. The absence of signal variation for both the Naph- and Phe-like channels mounted on the same MiniFluo-UV-1 sensor can be attributed either to sensitivity issues, to lower fluorescence intensity or to a contamination by environmental parameters (i.e. quenching). The background values of Naph-like concentrations recorded during the mission (i.e. ~20 ng/L) are higher than the PAH concentrations usually recorded in ocean waters that range between 1 to 10 ng/L. The strong expression of the Pyr-like signals compared with other PAH is remarkable considering that this pyrogenic component is not expected in natural oil seep systems. The few traces of Pyr reported in some crudes (Pampanin and Sydnes, 2013) combined with a much lower bioremediation efficiency may explain this signal (Stedmon et al., 2003; Ekperusi and Aigbodion, 2015).

5.2. Deep Chlorophyll Maximum in the sub-surface water

In the subsurface water, a consistent layer is enriched in chlorophyl-*a* (**Fig. 5**a), particulate matter (b_{bp700}; **Fig. 5**c) and to a more moderate extent in the humic-like component (**Fig. 5**b). The chlorophyll-*a* -like fluorescence shows a classical shape of a deep chlorophyll maximum (Cullen, 1982) at ~50 m. This corresponds fairly well to depth values of the deep chlorophyll maximum reported closer to the coast (Jourdin et al., 2006; Erickson et al., 2016), where the transition between photic and aphotic zones is shallower (Wasmund et al., 2005). High chlorophyll-*a*-like values suggest intense photosynthetic activity by the phytoplankton at the top of the first pycnocline (Zeng et al., 2017). Enrichment in phytoplankton concentrations is also coherent with high backscattering values in the first 100 m. The humic-like concentrations we observe (> 0.8 QSU) are rather high but remain coherent with similar coastal/upwelling systems (Nelson and Siegel, 2013), while low values detected near the surface can be associated with photobleaching (Del Vecchio and Blough, 2002; Miranda et al., 2018). This layer commonly hosts abundant biological processes, whose by-products have a similar fluorescence spectra signature to that of PAH (Tedetti et al., 2010; Jocis et al., 2014). For instance, heterotrophic bacteria (Tedetti et al., 2012) and phototrophic cyanobacteria reported in the sub-surface (within the deep chlorophyll maximum, below 75 m depth; *Synechococcus* and

366 *Prochlorococcus*; Zhao et al., 2017) have similar spectral signatures ($\lambda ex/\lambda em$ couple) compared to the PAH-like channel
367 (Ulloa et al., 2013; Gonzalez-Garcia et al., 2018). In these conditions, very high PAH-like concentrations detected in shallow
368 depths (~30 m; **Fig. 6**) would more likely be associated with biological processes than with a shallow hydrocarbon storage
369 layer.

370 **5.3. Horizontal anomaly in the oxygen minimum zone and interactions with biogeochemical parameters**

371 The intermediate layer of the Angolan waters corresponds to the South Atlantic oxygen minimum zone (OMZ) area (Mercier
372 et al., 2003; Karstensen et al., 2008; Mashifane et al., 2016; Schmidt and Eggert, 2016). In the northern half of the area (i.e.
373 after ~50 km in section distance), the core of the OMZ (300-500 m; **Fig. 4**e) is associated both with an increase in the Pyr-
374 (**Fig. 7**c), Flu- (**Fig. 7**d), humic-like and chlorophyll-*a*-like channels (**Fig. 5**a, b), and with a decrease in particulate matter load
375 and dissolved oxygen (DO) concentration (**Fig. 5**c). The layer between 250-350 m (i.e. above the Pyr-/Flu-like anomalies) is
376 characterized by slightly higher gradients of temperature and salinity, which is interpreted as the second thermo/pycnocline
377 (**Fig. 4**a, b).
378 The hypothesis of a layer of enhanced hydrocarbon content related to PAH-like concentrations in the intermediate layer is
379 supported by the density gradient modification (**Fig. 4**c). In these conditions, hydrocarbons released from the seafloor remain
380 stored and accumulate below the second thermo/pycnocline (**Fig. 6**d; Adalsteinsson et al., 2011; Camassa et al., 2013;
381 Landeau et al., 2014). The accumulation of PAH in the pycnocline vicinity has been already pointed out by Cyr et al. (2017).
382 Interactions between gas and water are inhibited in the gas hydrate stability zone in the water column, the depth of the upper
383 limit of these conditions depends on temperature, pressure, salinity and gas composition (**Fig. 8**a) but is usually estimated to
384 be 430 m below the sea surface (Kvenvolden and Barnard, 1983; Dholabhai et al., 1991; Rehder et al., 2002; McGinnis et al.,
385 2006; Sloan, 2003). Above this, hydrates dissociate and gases are rapidly oxidized ($2CH_4 + 4O_2 \rightarrow 2CO_2 + 4H_2O$). While the
386 top of the intermediate PAH-like anomaly corresponds to higher temperature gradients (**Fig. 8**a, b), the base correlates with
387 the dissociation depth of a classic mix of thermogenic gases (Tissot et Welte, 2012; Floodgate and Judd, 1992). In these
388 conditions, gas removal in the ascending hydrocarbon plume leads to a relative weighting of hydrocarbon mixing and to
389 dissolved oxygen (DO) depletion (**Fig. 8**b). This could support the hypothesis of a storage of heavier hydrocarbon
390 components above the top of the gas hydrate stability zone. In the deep waters of the Gulf of Mexico, Camilli et al. (2010)

made similar observations of a Naph trapped in a depleted DO layer after the Deep-Water Horizon blowout. In our case, the correlation between both the location and thickness of the PAH-like horizontal plume and the depths of the second thermocline, as well as the calculated hydrate-free transition layer forming physical boundaries suggests that PAH are entrapped in the OMZ.

The depleted DO layer is concomitant with an increase in humic-like and particle concentrations. The respiration of heterotrophic bacteria leads to an oxygen depletion linked with the oxidation/mineralization of particulate and dissolved organic matter (Joye et al., 2011; Kowalczuk et al., 2013). In parallel, oxidation is reported as a major removal process of PAH in the environment. Conversely, anoxic water enhances PAH preservation in the OMZ, which can support the hypothesis of horizontal PAH-like fluorescence anomalies in the 350-450 m intermediate water layer (*Fig*. 6 c, d). Collisional quenching effects can also contribute to increase the fluorescence signal. Even if the anti-correlation is not systematic, PAH-like signals coincide with a layer of lower DO concentrations and lower temperatures at these depths (*Fig*. 4a, d).

In the eastern South Pacific, the OMZ core at 300-400 m water depths is characterized by a humic-like and chlorophyll-*a*-like signal potentially related to the presence of microbial biomass (Whitmire et al., 2009) and by a b_{bp700} signal that can be associated with the presence of denitrifying and ammonium oxidizing bacteria (Garfield et al., 1983). In the northern half of our study area, apart from shallow waters, the highest particle concentrations occur at the upper and lower edges of the OMZ (*Fig*. 5c), which would reflect the maximal activity of bacteria at these depths.

Cyanobacteria (*Synechococcus* and *Prochlorococcus*) and sulphate reducers (prokaryotes: *Thioploca, Beggiatoa*) are involved in nitrogen recycling ($NH_4^+ + NO_2^- = N_2 + 2H_2O$; Farías et al., 2007) and sulphate reduction ($SO_4^{2-} + H_2O = H_2S + 2H_2O$; Gibson et al., 2003; Schunck et al., 2013), both biochemical processes occurring in OMZ conditions (Ulloa et al., 2012). These organisms and their biological by-products comprising humic-like organic matter have similar fluorescence properties compared with PAH, making it difficult to discriminate between biological products and dissolved hydrocarbons in the OMZ. Cyanobacteria are also reported to consume hydrocarbons (Cerniglia et al., 1980; Narro et al., 1992; Heider et al., 1998; Abed and Köster, 2005; Hazen et al., 2016), suggesting that both signals might be concomitant (Zhang et al., 2012). In our case, the increase of the b_{bp700} signal above and below the PAH-like horizontal anomaly that occurs alongside a

transition towards suboxic layers (DO> 45 µmol/kg) suggests the activity of an oxygen-dependent, hydrocarbon-consuming bacteria consortium (hydrocarbon oxidizing bacteria; Rosenberg and Gutnik, 1981).

In addition to hydrocarbon seepage, the intrusion of the Congo Plume waters in the study area can potentially have strong implications on organic matter and pollutant distribution. Congo waters show a particularly high content in dissolved organic matter (Nelson et al., 2010; Andrew et al., 2013), with concentrations up to 10.7 mg/L (Spencer et al., 2009). This significant river input of dissolved organic matter could thus also contribute to the humic- and chlorophyll-*a*-like anomalies observed in the OMZ core (**Fig. 5**).

5.4. Significance of spikes and columnar vertical anomalies

Columnar anomalies detected on Flu-like patterns of higher intensity occur at depths between 400 and 700 m. The signal remains low compared with the regional background, but with only a 3% concentration increase it is greater than the sensor precision (2%) and might therefore be related to environmental modifications. PAH-like vertical pipes are superimposed on the location of active oil seep areas, supporting the fact that the MiniFluo-UV sensors was detecting hydrocarbons. The maximum depth of investigation of the glider is 700 m while the water depths of the investigated area range between 1500 and 2100 m. It is possible that the dispersion of the oil during the ascent in the water may be at the origin of the low amplitudes of the PAH anomalies observed.

The detailed review of fluorescence data acquired during the mission reveals spike anomalies associated with important concentration increases in the PAH signal, either on the Phe-, Flu- or Pyr-like channels, which are usually considered as acquisition artifacts. Spikes appear locally as isolated spots or through a few adjacent glider profiles acquired during virtual mooring phases. Except for seep sites 1 and 5, PAH-like anomalies are all in close proximity to oil seep sites, suggesting a correlation between the recorded PAH signal and the presence of hydrocarbons (**Fig. 7**). As mentioned before, spikes mostly appear in one PAH optical channel, except at the location of seep site 3 where concomitant peaks are recorded for both the Flu- and Pyr-like channels (**Fig. 7**c, d). While the absence of PAH signals remains difficult to explain at site 1, the non-detection at seep site 5 can be explained by the fact that the glider only flew once over the seep area, therefore decreasing the probability of the glider to cross the hydrocarbon plume.

Considering that the MiniFluo-UV sensors can detect the dissolved portion of hydrocarbons only, their response to a contact with the non-aqueous liquid phase remains unknown. Sea surface slicks detected on SAR images testify to the presence of a liquid phase throughout the ascent in the water column. The MiniFluo-UV response to the presence of a liquid oil phase on the sensor measurement cells is unknown and yet plausible to explain spike signals. Optical paths being physically isolated by the sensor design, both UV channels might therefore be affected differently by the presence of oily-coated bubbles, thus explaining the independent response of the optical channels. In these conditions, spikes of the PAH signal would constitute a proxy for the presence of hydrocarbons in the water column.

6. Conclusions

This paper aimed to evaluate the effectiveness of fluorescence sensors in combination with biogeochemical and physical sensors mounted on submersible vehicles (gliders) to detect hydrocarbons in the natural oil seeping province of the Lower Congo basin. The mission was planned to monitor active natural oil seep sites during 20 days in conjunction with the acquisition of satellite images. The glider mission significantly improved our knowledge regarding hydro-physical conditions in the Lower Congo Basin, especially for the lateral and horizontal distribution of biogeochemical parameters and the evolution of the oxygen minimum zone in the area. Multiple polyaromatic (PAH-like) concentration anomalies were detected in relation with specific anomalous levels of dissolved oxygen and/or biogeochemical parameter responses. In the shallow waters, consistent PAH-like anomalies occurred in strict relationship with the Deep Chlorophyll Maximum, which is likely associated with microbial processes. Between 250 and 450 m, a PAH-like signal reveals the most interesting patterns. Here, the depletion of dissolved oxygen is associated with a horizontal plume characterized by increased concentrations of both pyrene and fluorene. The most conservative hypothesis concerning the origin of this fluorescence anomaly is the effect of bacterial processes. Another possibility is that this horizontal plume corresponds to dissolved hydrocarbons entrapped within stratified intermediate waters limited by the second thermo/pycnocline at the top and the hydrate dissociation layer at the bottom. Most conclusive observations refer to spike anomalies associated with a strong concentration variation of individual PAH-like fluorophores showing a good spatial correlation with oil seep sites evidenced by satellites. Deeper (400-

700 m water depth) columnar PAH-like anomalies associated with more moderate concentration changes could also correspond to vertical plumes of hydrocarbons.

Author contributions.

RJ, DD, FB designed the research. RJ, FB and OPdF analyzed the data. MT and MG guided the interpretation of the fluorescence signals. RJ prepared the manuscript with contributions of DD, MT, OPdF, LL, FB, MG and XDdM.

Competing interests.

The authors declare that they have no conflict of interest.

Acknowledgments

This work was performed in the context of a post-doctoral fellowship co-financed by the CNRS (Centre National de la Recherche Scientifique) and Total S.A. and in collaboration with the University of Perpignan (CEFREM, UMR 5110), France. The glider mission was funded by Total Research and Development with strong support from Total's affiliate in Angola. Copernicus Sentinel data 2017, processed by ESA, Radarsat satellite data processed by the Canadian Space Agency, Cosmo-Skymed processed by Telespazio and TerraSAR-X processed by the DLR. The authors thank the European Space Agency (Sentinel-1) for making open-access data available. . Madeleine Goutx thanks IFREMER for providing hosting facilities during the 2018-2019 period. Illustrations were made using Ocean Data View software.

References

Abed, R. M., & Köster, J.: (2005) The direct role of aerobic heterotrophic bacteria associated with cyanobacteria in the degradation of oil compounds. International biodeterioration & biodegradation, 55(1), 29-37, doi.org/10.1016/j.ibiod.2004.07.001

Abrams, M.A.: (2005) Significant of hydrocarbon seepage relative to petroleum generation and entrapment, Marine and Petroleum Geology 22, p. 457-477. doi.org/10.1016/j.marpetgeo.2004.08.003

Adalsteinsson, D., Camassa, R., Harenberg, S., Lin, Z., McLaughlin, R. M., Mertens, K., ... & MacFadyen, A. (2011). Subsurface trapping of oil plumes in stratification: laboratory investigations. *Geophys. Mon. Ser*, *195*, 257-261. doi.org/10.1029/2011GM001115

Alexander, J., Benford, D., Cockburn, A., Cravedi, J.P., Dogliotti, E., Di Domenico, A., Fernández-Cruz, M.L., Fink-Gremmels, J., Fürst, P., Galli, C., Grandjean, P., Gzyl, J., Heinemeyer, G., Johansson, N., Mutti, A., Schlatter, J., Van Leeuwen, R., Van Peteghem, C., Verger, P.: (2008) Scientific Opinion of the Panel on Contaminants in the Food Chain on a request from the European Commission on Polycyclic Aromatic Hydrocarbons in Food. The EFSA Journal (2008) 724, 1-114.

Alpers, W., & Espedal, H. A.: (2004) Oils and surfactants. In Jackson, C.R. and , Apel, J.R. (Eds) Synthetic aperture radar marine user's manual, National Environmental Satellite, Data, and Information Service (U.S.), pp 263-275. 016073214X (ISBN13: 9780160732140)

Andresen, K.J., & Huuse, M.: (2011) 'Bulls-eye' and polygonal faulting in the Lower Congo Basin: Relative timing and implications for fluid expulsion during shallow burial, Marine Geology 279, 111-127, doi.org/ 10.1016/j.margeo.2010.10.016.

Andresen, K.J., Huuse, M., Shödt., N.H., Clausen, F., & Seidler, L.: (2010) Hydrocarbon plumbing systems of salt minibasins offshore Angola revealed by three-dimensional seismic analysis, AAPG Bulletin, 95, 1039-1065, doi.org/10.1306/12131010046.

Andrew, A. A., Del Vecchio, R., Subramaniam, A., & Blough, N. V.: (2013) Chromophoric dissolved organic matter (CDOM) in the Equatorial Atlantic Ocean: optical properties and their relation to CDOM structure and source. Marine Chemistry, 148, 33-43, doi.org/10.1016/j.marchem.2012.11.001

Arhan, M., Mercier, H., & Park, Y. H.: (2003) On the deep water circulation of the eastern South Atlantic Ocean. Deep Sea Research Part I: Oceanographic Research Papers, 50(7), 889-916, doi.org/10.1016/S0967-0637(03)00072-4

Bern, T.I., Wahl, T., Anderssen, T., & Olsen, R.: (1992) Oil Spill detection using satellite based SAR: experience from a field Experiment, Proceedings First ERS-1 Symposium - Space at the Service of our Environment, 829 – 834.

508 Brekke, C., Solberg, A.H.S.: (2005) Oil spill detection by satellite remote sensing, Remote Sensing of Environment, 95, 1-
509 13, doi.org/10.1016/j.rse.2004.11.015.

510 Buiteveld, H., Hakvoort, J. H. M., & Donze, M. (1994, October). Optical properties of pure water. In *Ocean Optics XII*,
511 International Society for Optics and Photonics, 2258, pp. 174-183, doi.org/10.1117/12.190060

512 Burwood, R.: (1999) Angola: source rock control for Lower Congo Coastal and Kwanza Basin petroleum systems,
513 Geological Society, London, Special Publications,152, p181-184, doi.org/10.1144/GSL.SP.1999.153.01.12

514 Camassa, R., Khatri, S., McLaughlin, R., Mertens, K., Nenon, D., Smith, C., & Viotti, C.: (2013) Numerical simulations and
515 experimental measurements of dense-core vortex rings in a sharply stratified environment. Computational Science &
516 Discovery, 6 (1), doi.org/014001, 10.1088/1749-4699/6/1/014001

517 Camilli, R., Reddy, C. M., Yoerger, D. R., Van Mooy, B. A., Jakuba, M. V., Kinsey, J. C., ... & Maloney, J. V. (2010).
518 Tracking hydrocarbon plume transport and biodegradation at Deepwater Horizon. *Science*, *330*(6001), 201-204.
519 doi.org/10.1126/science.1195223Cerniglia, C. E., Gibson, D. T., & Van Baalen, C.: (1980) Oxidation of naphthalene by
520 cyanobacteria and microalgae. Microbiology, 116(2), 495-500. doi.org/10.1099/00221287-116-2-495

521 Clarke, G. L., & James, H. R.: (1939) Laboratory analysis of the selective absorption of light by sea water. JOSA, 29(2), 43-
522 55, doi.org/10.1364/JOSA.29.000043

523 Cole, G. A., Requejo, A.G., Ormerod, D., Yu, Z., & Clifford, A.: (2000) Petroleum geochemical assessment of the Lower
524 Congo Basin, in Mello, M.R., and Katz, B.J. (Eds), Petroleum systems of South Atlantic margins: AAPG Memoir 73, 325-
525 339.

526 Conmy, R. N., Del Castillo, C. E., Downing, B. D., & Chen, R. F.: (2014) Experimental design and quality assurance: In situ
527 fluorescence instrumentation. In Baker, A., Coble, P.G.,Reynolds, D.M., Lead, J., Spencer, R.GM. (Eds) Aquatic organic
528 matter fluorescence, pp 190-230. doi.org/10.1017/CBO9781139045452

529 Cullen, J. J.: (1982) The deep chlorophyll maximum: comparing vertical profiles of chlorophyll a. Canadian Journal of
530 Fisheries and Aquatic Sciences, 39(5), 791-803. doi.org/10.1139/f82-108

Cullen, J. J., & Lewis, M. R. (1995). Biological processes and optical measurements near the sea surface: Some issues relevant to remote sensing. Journal of Geophysical Research: Oceans, 100(C7), 13255-13266.

Cyr, F., Tedetti, M., Besson, F., Beguery, L., Doglioli, A. M., Petrenko, A. A., & Goutx, M.: (2017) A New Glider-Compatible Optical Sensor for Dissolved Organic Matter Measurements: Test Case from the NW Mediterranean Sea. Frontiers in Marine Science, 4, 89. doi.org/10.3389/fmars.2017.00089

Cyr, F., Tedetti, M., Besson, F., Bhairy, N., & Goutx, M.: (2019) A glider-compatible optical sensor for the detection of polycyclic aromatic hydrocarbons in the marine environment. Frontiers in Marine Science, 6, 110. doi.org/10.3389/fmars.2019.00110

Dabestani, R., Ivanov, I.,: (1999). A Compilation of physical, spectroscopic and photophyisical properties of polycyclic aromatic hydrocarbons. Photochemistry and Photobiology, 70, 10–34.

Dall'Olmo, G., Westberry, T. K., Behrenfeld, M. J., Boss, E., & Slade, W. H.: (2009) Significant contribution of large particles to optical backscattering in the open ocean. Biogeosciences, 6(6), 947.

Danielsen, K. M., Chin, Y. P., Buterbaugh, J. S., Gustafson, T. L., & Traina, S. J.: (1995) Solubility enhancement and fluorescence quenching of pyrene by humic substances: The effect of dissolved oxygen on quenching processes. Environmental science & technology, 29(8), 2162-2165, doi.org/10.1021/es00008a042

Davis, R., Eriksen, C., Jones, C.: (2002). Autonomous Buoyancy-Driven Underwater Gliders, In: Griffiths, G. (Ed.), Technology and Applications of Autonomous Underwater Vehicles. CRC Press, pp. 37–58, doi.org/10.1201/9780203522301

Del Vecchio, R., & Blough, N. V.: (2002) Photobleaching of chromophoric dissolved organic matter in natural waters: kinetics and modeling. Marine Chemistry, 78(4), 231-253, doi.org/10.1016/S0304-4203(02)00036-1

Dholabhai, P. D., Englezos, P., Kalogerakis, N., & Bishnoi, P. R.: (1991) Equilibrium conditions for methane hydrate formation in aqueous mixed electrolyte solutions. The Canadian Journal of Chemical Engineering, 69(3), 800-805, doi.org/10.1002/cjce.5450690324

553 Dhont, D., Jatiault, R., & Lattes, P. (2019). Combined Use of SAR and Underwater Gliders for Oil Seeps Detection.
554 IGARSS 2019 - 2019 IEEE International Geoscience and Remote Sensing Symposium. doi:10.1109/igarss.2019.8898602

555 Doi, T., Tozuka, T., Sasaki, H., Masumoto, Y., & Yamagata, T.: (2007) Seasonal and interannual variations of oceanic
556 conditions in the Angola Dome. Journal of Physical Oceanography, 37(11), 2698-2713, doi.org/10.1175/2007JPO3552.1

557 Dupont, L.M.: (2013) The Congo Deep-Sea fan as an archive of Quaternary change in Africa and the Eastern Tropical South
558 Atlantic (a review), In Kneller, B.C., Ole, J., Martinsen, J., McCaffrey, B. (Eds) External Controls on Deep-Water
559 Depositional Systems, SEPM Special Publication No. 92, pp 79-87.

560 Dupré, S., Berger, L., Le Bouffant, N., Scalabrin, C., & Bourillet, J. F.: (2014) Fluid emissions at the Aquitaine Shelf (Bay
561 of Biscay, France) A biogenic origin or the expression of hydrocarbon leakage? Continental Shelf Research, 88, 24-33,
562 doi.org/10.1016/j.csr.2014.07.004

563 Ekperusi, O. A., & Aigbodion, F. I.: (2015) Bioremediation of petroleum hydrocarbons from crude oil-contaminated soil
564 with the earthworm: Hyperiodrilus africanus. 3 Biotech, 5(6), 957-965, doi.org/10.1007/s13205-015-0298-1

565 Erickson, Z. K., Thompson, A. F., Cassar, N., Sprintall, J., & Mazloff, M. R. (2016). An advective mechanism for deep
566 chlorophyll maxima formation in southern Drake Passage. *Geophysical Research Letters*, *43*(20), 10-846,
567 doi:10.1002/2016GL070565.

568 Espedal, H.A., & Johannessen, O.M.: (2000) Detection of oil spills near offshore installations using synthetic aperture radar
569 (SAR), International Journal of Remote Sensing, 21:11, 2141-2144, doi.org/10.1080/01431160050029468.

570 Espedal, H.A., & Wahl, T.: (1999) Satellite SAR oil spill detection using wind history information, International Journal of
571 Remote Sensing, 20, 49-65, doi.org/10.1080/014311699213596

572 Farías, L., Paulmier, A., & Gallegos, M.: (2007) Nitrous oxide and N-nutrient cycling in the oxygen minimum zone off
573 northern Chile. Deep Sea Research Part I: Oceanographic Research Papers, 54(2), 164-180,
574 doi.org/10.1016/j.dsr.2006.11.003

575 Ferdinand, O. D., Friedrichs, A., Miranda, M. L., Voß, D., & Zielinski, O.: (2017, June) Next generation fluorescence sensor
576 with multiple excitation and emission wavelengths—NeXOS MatrixFlu-UV. In OCEANS 2017-Aberdeen, IEEE, pp. 1-6,
577 DOI.org/10.1109/OCEANSE.2017.8084809

578 Ferretto, N., Tedetti, M., Guigue, C., Mounier, S., Redon, R., & Goutx, M.: (2014) Identification and quantification of
579 known polycyclic aromatic hydrocarbons and pesticides in complex mixtures using fluorescence excitation–emission
580 matrices and parallel factor analysis. Chemosphere, 107, 344-353, doi.org/10.1016/j.chemosphere.2013.12.087

581 Fingas, M., & Brown, C.: (2014) Review of oil spill remote sensing. Marine pollution bulletin, 83(1), 9-23,
582 doi.org/10.1016/j.marpolbul.20104.03.059.

583 Floodgate, G.D., & Judd, A.G.: (1992) The origins of shallow gas, Continental Shelf Research, 12 (10), 1145 – 1156,
584 doi.org/10.1016/0278-4343(92)90075-U

585 Gauthier, T. D., Shane, E. C., Guerin, W. F., Seitz, W. R., & Grant, C. L.: (1986) Fluorescence quenching method for
586 determining equilibrium constants for polycyclic aromatic hydrocarbons binding to dissolved humic materials.
587 Environmental Science & Technology, 20(11), 1162-1166, doi.org/10.1021/es00153a012

588 Garcia-Pineda, O., MacDonald, I., Zimmer, B., Shedd, B., & Roberts, H.: (2010) Remote-sensing evaluation of geophysical
589 anomaly sites in the outer continental slope, northern Gulf of Mexico, Deep-Sea research II, 57, 1859-1869,
590 doi.org/10.1016/j.dsr2.2010.05.005.

591 Garfield, P. C., Packard, T. T., Friederich, G. E., & Codispoti, L. A.: (1983) A subsurface particle maximum layer and
592 enhanced microbial activity in the secondary nitrite maximum of the northeastern tropical Pacific Ocean. Journal of Marine
593 Research, 41(4), 747-768, doi.org/10.1357/002224083788520496

594 Garzoli, S. L., Dong, S., Fine, R., Meinen, C. S., Perez, R. C., Schmid, C., .. & Yao, Q.: (2015) The fate of the deep western
595 boundary current in the South Atlantic. Deep Sea Research Part I: Oceanographic Research Papers, 103, 125-136,
596 doi.org/10.1016/j.dsr.2015.05.008

597 Gay, A., Lopez, M., Berndt, C., & Séranne, M.: (2007) Geological controls on focused fluid flow associated with seafloor
598 seeps in the Lower Congo Basin, Marine Geology 244, 68 – 92, doi.org/10.1016/j.margeo.2007.06.003

599 Gibson, R. N., & Atkinson, R. J. A.: (2003) Oxygen minimum zone benthos: adaptation and community response to
600 hypoxia. In Gibson, R.N., Atkinso, R.J.A., Oceanography and Marine Biology, An Annual Review, 41, pp 1-45.

601 González-Gaya B, Fernández-Pinos M-C, Morales L, Méjanelle L, Abad E, et al.: (2016) High atmosphere–ocean exchange
602 of semivolatile aromatic hydrocarbons. Nature Geoscience 9: 438–442, doi.org/10.1038/ngeo2714

603 González-García, C., Forja, J., González-Cabrera, M. C., Jiménez, M. P., & Lubián, L. M.: (2018) Annual variations of total
604 and fractionated chlorophyll and phytoplankton groups in the Gulf of Cadiz. Science of the Total Environment, 613, 1551-
605 1565, doi.org/10.1016/j.scitotenv.2017.08.292

606 GROOM (Gliders for Research, Ocean Observation and Management) FP7 project: (2014) Scientific report on existing
607 sensors to be integrated on gliders for biogeochemical and biological applications and underwater data transmission,
608 Deliverable D3.5, www.groomfp7.eu/lib/exe/fetch.php?media=public:deliverables:groom_d_3_05_upmc.pdf.

609 Greinert, J., Artemov, Y., Egorov, V., De Batist, M., & McGinnis, D.: (2006) 1300-m-high rising bubbles from mud
610 volcanoes at 2080m in the Black Sea: Hydroacoustic characteristics and temporal variability, Earth and Planetary Science
611 Letters, 244, 1–15, doi.org/10.1016/j.epsl.2006.02.011.

612 Guiraud, M., Buta-Neto, A., & Quesne, D.: (2010) Segmentation and differential post-rift uplift at the Angola margin as
613 recorded by the transform-rifted Benguela and oblique-to-orthogonal-rifted Kwanza basins. Marine and Petroleum Geology,
614 27(5), 1040-1068, doi.org/10.1016/j.marpetgeo.2010.01.017

615 Hardman-Mountford, N.J., Richardson, A.J., Agenbag, J.J., Hagen, E., Nykjaer, L., Shillington, F.A., & Villacastin, C.:
616 (2003) Ocean climate of the South Esat Atlantic observed from satellite data and wind models, Progress in Oceanography,
617 59, 181-221, doi.org/10.1016/j.pocean.2003.10.001

618 Hazen, T. C., Prince, R. C., & Mahmoudi, N.: (2016) Marine oil biodegradation. *Environ. Sci. Technol.*, 50(5), 2121–2129,
619 doi.org/10.1021/acs.est.5b03333

620 Heider, J., Spormann, A. M., Beller, H. R., & Widdel, F.: (1998) Anaerobic bacterial metabolism of hydrocarbons. FEMS
621 Microbiology Reviews, 22(5), 459-473, doi.org/10.1111/j.1574-6976.1998.tb00381.x

622 Hopkins, J., Lucas, M., Dufau, C., Sutton, M., & Stum, J.: (2013) Detection and variability of the Congo River plume from
623 satellite derived sea surface temperature, salinity, ocean colour and sea level. Remote Sensing of Environment, 139, 365-
624 385, doi.org/10.1016/j.rse.2013.08.015

625 Hudec, M. R., & Jackson, M. P.: (2004) Regional restoration across the Kwanza Basin, Angola: Salt tectonics triggered by
626 repeated uplift of a metastable passive margin. AAPG bulletin, 88(7), 971-990, doi.org/10.1306/02050403061

627 Hylland, K.: (2006) Polycyclic aromatic hydrocarbon (PAH) ecotoxicology in marine ecosystems. Journal of Toxicology
628 and Environmental Health, Part A, 69(1-2), 109-123, doi.org/10.1080/15287390500259327

629 IOC, SCOR and IAPSO, 2010: The international thermodynamic equation of seawater – 2010: Calculation and use of
630 thermodynamic properties. Intergovernmental Oceanographic Commission, Manuals and Guides, 56, UNESCO, 196 pp,
631 http://www.teos-10.org/pubs/TEOS-10_Manual.pdf

632 Jatiault, R., Dhont, D., Loncke, L., & Dubucq, D.: (2017) Monitoring of natural oil seepage in the Lower Congo Basin using
633 SAR observations. Remote Sensing of Environment, 191, 258 - 272. doi.org/10.1016/j.rse.2017.01.031.

634 Jatiault, R., Dhont, D., Loncke, L., de Madron, X. D., Dubucq, D., Channelliere, C., & Bourrin, F.: (2018) Deflection of
635 natural oil droplets through the water column in deep-water environments: The case of the Lower Congo Basin. Deep Sea
636 Research Part I: Oceanographic Research Papers, 136, 44-61, doi.org/10.1016/j.dsr.2018.04.009

637 Jatiault, R., Loncke, L., Dhont, D., Imbert, P., & Dubucq, D. (2019a). Geophysical characterisation of active thermogenic oil
638 seeps in the salt province of the lower Congo basin part I: Detailed study of one oil-seeping site. Marine and Petroleum
639 Geology, 103, 753-772., doi.org/10.1016/j.marpetgeo.2018.11.026.

640 Jatiault, R., Dhont, D., Loncke, L., Dubucq, D., Imbert, P. (2019b). Geophysical characterisation of active thermogenic oil
641 seeps in the salt province of the Lower Congo Basin. Part II: A regional validation. Marine and Petroleum Geology. doi:
642 https://doi.org/10.1016/j.marpetgeo.2019.02.002

643 Jenkins, S.A., & D'Spain, G.: (2016) Autonomous underwater gliders, in: Dhanak, M.R. and Xiros, N.I. (eds.), Springer
644 Handbook of Ocean Engineering, pp. 301–322, doi.org/10.1007/978-3-319-16649-0_12

645 Jones, D. O., Walls, A., Clare, M., Fiske, M. S., Weiland, R. J., O'Brien, R., & Touzel, D. F. (2014). Asphalt mounds and
646 associated biota on the Angolan margin. *Deep Sea Research Part I: Oceanographic Research Papers*, *94*, 124-136,
647 doi.org/10.1016/j.dsr.2014.08.010

648 Jourdin, F., Froidefond, J. M., Loyer, S., Lefèvre, C., Mayoyas, Y. K., Vrignaud, C., & Kolodziejczyk, N.: (2006) Measuring
649 upper ocean turbidity off Congo and Gabon coasts. Proceedings of Caracterisation du Milieu Marin, 6, 16-19.

650 Joye, S. B., MacDonald, I. R., Leifer, I., & Asper, V.: (2011) Magnitude and oxidation potential of hydrocarbon gases
651 released from the BP oil well blowout. Nature Geoscience, 4(3), 160, doi.org/10.1038/ngeo1067

652 Karstensen, J., Stramma, L., & Visbeck, M.: (2008) Oxygen minimum zones in the eastern tropical Atlantic and Pacific
653 oceans. Progress in Oceanography, 77(4), 331-350, doi.org/10.1016/j.pocean.2007.05.009

654 Kim, J., Park, Y., Lee, S., & Lee, Y. K.: (2014) Underwater glider navigation error compensation using sea current data.
655 IFAC Proceedings Volumes, 47(3), 9661-9666, doi.org/10.3182/20140824-6-ZA-1003.01508

656 Korotenko, K. A.: (2016) High-Resolution Numerical Model for Predicting the Transport and Dispersal of Oil Spill in Result
657 of Accidental Deepwater Blowout in the Black Sea. In The 26th International Ocean and Polar Engineering Conference.
658 International Society of Offshore and Polar Engineers, doi.org/10.3319/TAO.2009.04.24.01(IWNOP)

659 Kowalczuk, P., Tilstone, G. H., Zabłocka, M., Röttgers, R., & Thomas, R.: (2013) Composition of dissolved organic matter
660 along an Atlantic Meridional Transect from fluorescence spectroscopy and Parallel Factor Analysis. Marine Chemistry, 157,
661 170-184, doi.org/10.1016/j.marchem.2013.10.004

662 Kvenvolden, K. A., & Barnard, L. A.: (1983) Hydrates of natural gas in continental margins. Studies in continental margin
663 geology, 34, 631-640.

664 Landeau, M., Deguen, R., & Olson, P.: (2014) Experiments on the fragmentation of a buoyant liquid volume in another
665 liquid. Journal of Fluid Mechanics, 749, 478-518, doi.org/10.1017/jfm.2014.202

Lass, H.U., Schmidt, M., Mohrholz, V., & Nausch, G.: (2000) Hydrographic and current measurements in the area of the Angola-Benguela front. Journal of Physical Oceanography, 30, 2589-2609, doi.org/10.1175/1520-0485(2000)030<2589:HACMIT>2.0.CO;2

Leifer, I., Lehr, W.J., Simecek-Beatty, D., Bradley, E., Clark, R;, Dennison, P., Hu, Y, Matheson, S., Jones, C.E., Holt, B., Reif, M., Roberts, D.A., Svejkovsky, J., Swayze, G., & Wozencraft, J.: (2012) State of the art satellite and airborne marine oil spill remote sensing: Application to the BP Deepwater Horizon oil spill, Remote Sensing of Environment, 124, 185-209, doi.org/10.1016/j.rse.2012.03.024

Loranger, S., Bassett, C., Cole, J. P., Boyle, B., & Weber, T. C.: (2018) Acoustically relevant properties of four crude oils at oceanographic temperatures and pressures. The Journal of the Acoustical Society of America, 144(5), 2926-2936, doi.org/10.1121/1.5078606

Lynn, R.J.: (1971) On Potential Density in the Deep South Atlantic Ocean, Journal of Marine research, 29, 171 – 177.

MacDonald, I.R., Garcia-Pineda, O., Beet, A., Daneshgar Asl, S., Feng, L., Graettinger, G., French-McCay, D., Holmes, J., Hu, C., Huffer, F., Leifer, I., Muller-Karger, F., Solow, A., Silva, M., & Swayze, G.: (2015) Natural and unnatural oil slicks in the Gulf of Mexico. Journal of Geophysical Research: Oceans, 120(12), 8364-8380, doi.org/10.1002/2015JC011062

MacDonald, I.R., Leifer, I., Sassen, R., Stine, P., Mitchell, R., & Guinasso, J.N.: (2002) Transfer of hydrocarbons from natural seeps to the water column and atmosphere. Geofluids, 2, 95-107, doi.org/10.1046/j.1468-8123.2002.00023.x

Marton, G.L., Tari, G. C., & Lehmann, C. T.: (2000) Evolution of the Angolan Passive Margin, West Africa, With Emphasis on Post-Salt Structural Styles. In Mohriak, W., Talwani, M. (Eds) Atlantic rifts and continental margins, pp 129-149.

Marton, G., Carpenter, D., & Greg, S.: (2004) Salt Tectonics of the Continent-Ocean Transition, Deep-Water Angola: Concepts, Applications and Case Studies for the 21st Century, 24th Annual GCSSEPM Foundation Bob F. Perkins Research Conference pp.709 – 735.

687 Mashifane, T. B., Vichi, M., Waldron, H. N., Machu, E., & Garcon, V.: (2016) Modelling nitrite dynamics and associated
688 feedback processes in the Benguela oxygen minimum zone. Continental Shelf Research, 124, 200-212,
689 doi.org/10.1016/j.csr.2016.05.004

690 Mazeika, P. A.: (1967) Thermal domes in the eastern tropical Atlantic Ocean. Limnology and Oceanography, 12(3), 537-
691 539, doi.org/10.4319/lo.1967.12.3.0537

692 McGinnis, D. F., Greinert, J., Artemov, Y., Beaubien, S. E., & Wüest, A.: (2006) Fate of rising methane bubbles in stratified
693 waters: How much methane reaches the atmosphere?, Journal of Geophysical Research, 11, 1 – 15, doi.org/
694 10.1029/2005JC003183

695 Mercier, H., Arhan, M., & Lutjeharms, J. R.: (2003) Upper-layer circulation in the eastern Equatorial and South Atlantic
696 Ocean in January–March 1995. Deep Sea Research Part I: Oceanographic Research Papers, 50(7), 863-887,
697 doi.org/10.1016/S0967-0637(03)00071-2.

698 Meyer, D.: (2016) Glider technology for ocean observations: a review. Ocean Sci. Discuss, 26, doi.org/10.5194/os-2016-40

699 Milkov, A. V., Sassen, R., Novikova, I., & Mikhailov, E.: (2000) Gas hydrates at minimum stability water depths in the Gulf
700 of Mexico: significance to geohazard assessment.

701 Miranda, M. L., Mustaffa, N. I. H., Robinson, T. B., Stolle, C., Ribas-Ribas, M., Wurl, O., Zielinski, Blomquist, B.: (2018)
702 Influence of solar radiation on biogeochemical parameters and fluorescent dissolved organic matter (FDOM) in the sea
703 surface microlayer of the southern coastal North Sea. Elementa: Science of the Anthropocene, 6.Moroshkin, K.V., Bunov,
704 V.A., & Bulatov, R.P.: (1970) Water circulation in the eastern South Atlantic Ocean. Oceanology, 10, 27–34.

705 Mortier, L., Karstensen, J., Testor, P., Hayes, D., Mauri, E., Heywood, K., & Mortier, L.: (2012). Gliders for Research,
706 Ocean Observation and Management-GROOM. *EGUGA*, 5254, 2012EGUGA..14.5254M

707 Narro, M. L., Cerniglia, C. E., Van Baalen, C. H. A. S. E., & Gibson, D. T.: (1992) Metabolism of phenanthrene by the
708 marine cyanobacterium Agmenellum quadruplicatum PR-6. Applied and environmental microbiology, 58(4), 1351-1359.

709 Nelson, N. B., & Siegel, D. A.: (2013) The global distribution and dynamics of chromophoric dissolved organic matter.
710 Annual review of marine science, 5, 447-476, doi.org/10.1146/annurev-marine-120710-100751

711 Nelson, N. B., Siegel, D. A., Carlson, C. A., & Swan, C. M.: (2010) Tracing global biogeochemical cycles and meridional
712 overturning circulation using chromophoric dissolved organic matter. Geophysical Research Letters, 37(3),
713 doi.org/10.1029/2009GL042325

714 Nicholson, J.W., & Healey, AJ.J.: (2008) The present state of autonomous underwater vehicle (AUV) applications and
715 technologies. In Kocak, D.M., Crout, R. (Eds) Marine Technology Scientific Journal, 42(1), pp 44-51.

716 Nijegorodov, N., Vasilenko, V., Monowe, P., & Masale, M.: (2009) Systematic investigation of the influence of methyl
717 groups upon fluorescence parameters and the intersystem crossing rate constant of aromatic molecules. Spectrochimica Acta
718 Part A: Molecular and Biomolecular Spectroscopy, 74(1), 188-194, doi.org/10.1016/j.saa.2009.06.003

719 Osburn, C. L., Del Vecchio, R., & Boyd, T. J.: (2014) Physicochemical effects on dissolved organic matter fluorescence in
720 natural waters. In Coble, P.C., Lead, J., Baker, A., Reynolds, D.M, Spencer, R.G.M. (Eds) Aquatic organic matter
721 fluorescence, pp 233-277.

722 Owens, W. B., & Millard Jr, R. C.: (1985) A new algorithm for CTD oxygen calibration. Journal of Physical Oceanography,
723 15(5), 621-631, doi.org/10.1175/1520-0485(1985)015<0621:ANAFCO>2.0.CO;2

724 Pampanin, D. M., & Sydnes, M. O.: (2013) Polycyclic aromatic hydrocarbons a constituent of petroleum: presence and
725 influence in the aquatic environment. In Kutcherov, V., Kolesnikov, A. (Eds) Hydrocarbon, 5, pp. 83-118

726 Para, J., Coble, P. G., Charrière, B., Tedetti, M., Fontana, C., & Sempéré, R.: (2010) Fluorescence and absorption properties
727 of chromophoric dissolved organic matter (CDOM) in coastal surface waters of the northwestern Mediterranean Sea,
728 influence of the Rhône River. Biogeosciences, 7(12), 4083-4103, doi.org/10.5194/bg-7-4083-2010

729 Parlanti, E., Wörz, K., Geoffroy, L., & Lamotte, M.: (2000) Dissolved organic matter fluorescence spectroscopy as a tool to
730 estimate biological activity in a coastal zone submitted to anthropogenic inputs. Organic geochemistry, 31(12), 1765-1781,
731 doi.org/10.1016/S0146-6380(00)00124-8

Peterson, R.G., & Stramma, L.: (1991) Upper-level circulation in the South Atlantic Ocean, Progress in Oceanography, 26, 1-73, doi.org/10.1016/0079-6611(91)90006-8

Pope, R. M., & Fry, E. S.: (1997) Absorption spectrum (380–700 nm) of pure water. II. Integrating cavity measurements. Applied optics, 36(33), 8710-8723, doi.org/10.1364/AO.36.008710

Prince, R. C., Lessard, R. R., & Clark, J. R.: (2003) Bioremediation of marine oil spills. Oil & Gas Science and Technology, 58(4), 463-468, doi.org/10.2516/ogst:2003029

Rehder, G., Brewer., P.W., Peltzer, E.T., & Friederich, G.: (2002) Enhanced lifetime of methane bubble streams within the deep ocean, Geophysical Research Letters, 29:15, 1731, doi.org/10.1029/2001GL013966

Rosenberg, E., & Gutnick, D. L.: (1981) The hydrocarbon-oxidizing bacteria. In Starr,P., Stolp, H., Trüper, H.G., Balows, A., Schlegel, H.G. (Eds) The prokaryotes, Springer, Berlin, Heidelberg, pp 903-912

Rudnik-Schöneborn, S., & Zerres, K.: (2004) Outcome in pregnancies complicated by myotonic dystrophy: a study of 31 patients and review of the literature. European Journal of Obstetrics & Gynecology and Reproductive Biology, 114(1), 44-53, doi.org/10.1016/j.ejogrb.2003.11.025

Sassen, R., Sweet, S. T., Milkov, A. V., DeFreitas, D. A., Salata, G. G., & McDade, E. C.: (1999) Geology and geochemistry of gas hydrates, central Gulf of Mexico continental slope.

Schunck, H., Lavik, G., Desai, D. K., Großkopf, T., Kalvelage, T., Löscher, C. R., ... & Rosenstiel, P.: (2013) Giant hydrogen sulfide plume in the oxygen minimum zone off Peru supports chemolithoautotrophy. PLoS One, 8(8), e68661, doi.org/10.1371/journal.pone.0068661

Schmidt, M., & Eggert, A.: (2016) Oxygen cycling in the northern Benguela Upwelling System: Modelling oxygen sources and sinks. Progress in Oceanography, 149, 145-173, doi.org/10.1016/j.pocean.2016.09.004

Schoellkopf, N. B., & Patterson, B.A.: (2000) Petroleum systems of offshore, Cabinda, Angola, in M. R. Mello and B. J. Katz, Petroleum systems of South Atlantic margins: AAPG Memoir 73, 361–376.

754 Shannon, L.V.: (2001) Benguela Current, in Ocean Currents: a derivative of encyclopedia of Ocean Sciences, 2nd Edition,
755 23-34.

756 Sloan, E. D.: (2003) Fundamental principles and applications of natural gas hydrates. Nature, 426 (6964), 353-363.

757 Spencer, R. G., Stubbins, A., Hernes, P. J., Baker, A., Mopper, K., Aufdenkampe, A. K., .. & Six, J.: (2009) Photochemical
758 degradation of dissolved organic matter and dissolved lignin phenols from the Congo River. Journal of Geophysical
759 Research: Biogeosciences, 114(G3).

760 Stedmon, C. A., & Cory, R. M.: (2014) Biological origins and fate of fluorescent dissolved organic matter in aquatic
761 environments. In Coble, P.C., Lead, J., Baker, A., Reynolds, D.M, Spencer, R.G.M. (Eds) Aquatic organic matter
762 fluorescence, pp 278-299.

763 Stedmon, C. A., Markager, S., & Bro, R. (2003). Tracing dissolved organic matter in aquatic environments using a new
764 approach to fluorescence spectroscopy. Marine Chemistry, 82(3-4), 239–254. doi:10.1016/s0304-4203(03)00072-0

765 Stramma, L., & England M.: (1999) On the water masses and mean circulation of the South Atlantic Ocean, Journal of
766 Geophysical research, 104, 20863 – 20883.

767 Stramma, L., Prince, E. D., Schmidtko, S., Luo, J., Hoolihan, J. P., Visbeck, M., ... & Körtzinger, A.: (2012) Expansion of
768 oxygen minimum zones may reduce available habitat for tropical pelagic fishes. Nature Climate Change, 2(1), 33-37,
769 doi.org/10.1038/nclimate1304

770 Stramma, L., & Schott, F.: (1999) The mean flow field of the tropical Atlantic Ocean. Deep Sea Research Part II: Topical
771 Studies in Oceanography, 46(1), 279-303.

772 Tedetti, M., Guigue, C., & Goutx, M.: (2010) Utilization of a submersible UV fluorometer for monitoring anthropogenic
773 inputs in the Mediterranean coastal waters. Marine pollution bulletin, 60(3), 350-362,
774 doi.org/10.1016/j.marpolbul.2009.10.018

775 Tedetti, M., Longhitano, R., Garcia, N., Guigue, C., Ferretto, N., & Goutx, M.: (2012) Fluorescence properties of dissolved
776 organic matter in coastal Mediterranean waters influenced by a municipal sewage effluent (Bay of Marseilles, France).
777 Environmental Chemistry, 9(5), 438-449, doi.org/10.1071/EN12081

778 Testor, P., Meyers, G., Pattiaratchi, C., Bachmayer, R., Hayes, D., Pouliquen, S., & Mortier, L.: (2010) Gliders as a
779 component of future observing systems. OceanObs' 09.

780 Teuber, L., Schukat, A., Hagen, W., & Auel, H.: (2013) Distribution and ecophysiology of calanoid copepods in relation to
781 the oxygen minimum zone in the eastern tropical Atlantic. PloS one, 8(11), e77590, doi.org/10.1371/journal.pone.0077590

782 Ukwe, C.N., Ibe, C.A., & Sherman, K.: (2006) A sixteen-country mobilization for sustainable fisheries in the Guinea Current
783 Large Marine Ecosystem, Ocean & Coastal Management 49, 385–412, doi.org/10.1016/j.ocecoaman.2006.04.006

784 Ulloa, O., Canfield, D. E., DeLong, E. F., Letelier, R. M., & Stewart, F. J. (2012). Microbial oceanography of anoxic oxygen
785 minimum zones. *Proceedings of the National Academy of Sciences*, *109*(40), 15996-16003,
786 doi.org/10.1073/pnas.1205009109

787 Wade, T. L., Sweet, S. T., Sericano, J. L., Guinasso, N. L., Diercks, A.-R., Highsmith, R. C., … Joye, S. B. (2011). *Analyses*
788 *of Water Samples From the Deepwater Horizon Oil Spill: Documentation of the Subsurface Plume. Geophysical Monograph*
789 *Series, 77–82.* doi:10.1029/2011gm001103

790 Wasmund, N., Lass, H. U., & Nausch, G.: (2005) Distribution of nutrients, chlorophyll and phytoplankton primary
791 production in relation to hydrographic structures bordering the Benguela-Angolan frontal region. African Journal of Marine
792 Science, 27(1), 177-190, doi.org/10.2989/18142320509504077

793 Whitmire, A. L., Letelier, R. M., Villagrán, V., & Ulloa, O.: (2009) Autonomous observations of in vivo fluorescence and
794 particle backscattering in an oceanic oxygen minimum zone. Optics express, 17(24), 21992-22004,
795 doi.org/10.1364/OE.17.021992

796 Wilson, R. D., Monaghan, P.H., Osanik, A., Price, L., C., & Rogers, M. A.: (1973) Estimate of Annual input of Petroleum to
797 the Marine Environment from Natural Marine Seepage. Trans. Gulf Coast Assoc. Geological Societies, 23, 182-193.

798 Wozniak, B., & Dera, J.: (2007) Light absorption in sea water (Vol. 33). New York, NY, USA: Springer, 453p

799 Wood and Stephen.: (2009) Autonomous underwater gliders. In Inzartsev, A.V. (Ed) Underwater vehicles, 499-524. doi.org/
800 10.5772/6718.

801 Wright, J. J., Konwar, K. M., & Hallam, S. J.: (2012) Microbial ecology of expanding oxygen minimum zones. Nature
802 Reviews Microbiology, 10(6), 381–394, doi.org/10.1038/nrmicro2778

803 Xu, K. X., Cheng, P. F., Zhao, J., & Wang, C. J.: (2011) Enantioselective fluorescent sensors for amino acid derivatives
804 based on BINOL bearing S-tryptophan unit: synthesis and chiral recognition. Journal of fluorescence, 21(3), 991-1000,
805 doi.org/10.1007/s10895-009-0585-5

806 Zeng, C., Zeng, T., Fischer, A. M., & Xu, H.: (2017) Fluorescence-based approach to estimate the chlorophyll-a
807 concentration of a phytoplankton bloom in ardley cove (Antarctica). Remote Sensing, 9(3), 210, doi.org/10.3390/rs9030210

808 Zhang, D., Muller, J. P., Lavender, S., Walton, D., & Dartnell, L. R.: (2012) Fluorescent analysis of photosynthetic microbes
809 and polycyclic aromatic hydrocarbons linked to optical remote sensing. International Archives of the Photogrammetry,
810 Remote Sensing and Spatial Information Sciences, 39, 555-559 , doi.org/10.5194/isprsarchives-XXXIX-B8-555-2012

811 Zhao, Z., Gonsior, M., Luek, J., Timko, S., Ianiri, H., Hertkorn, N., .. & Chen, F.: (2017) Picocyanobacteria and deep-ocean
812 fluorescent dissolved organic matter share similar optical properties. Nature communications, 8, 15284,
813 doi.org/10.1038/ncomms15284

814 Zielinski, O., Busch, J. A., Cembella, A. D., Daly, K. L., Engelbrektsson, J., Hannides, A. K., & Schmidt, H. (2009).
815 Detecting marine hazardous substances and organisms: sensors for pollutants, toxins, and pathogens. *Ocean Science*, *5*(3),
816 329, doi.org/10.5194/os-5-329-2009

817 Zielinski, O., Rüssmeier, N., Ferdinand, O., Miranda, M., & Wollschläger, J.: (2018) Assessing Fluorescent Organic Matter
818 in Natural Waters: Towards In Situ Excitation–Emission Matrix Spectroscopy. Applied Sciences, 8(12), 2685,
819 doi.org/10.3390/app8122685

820

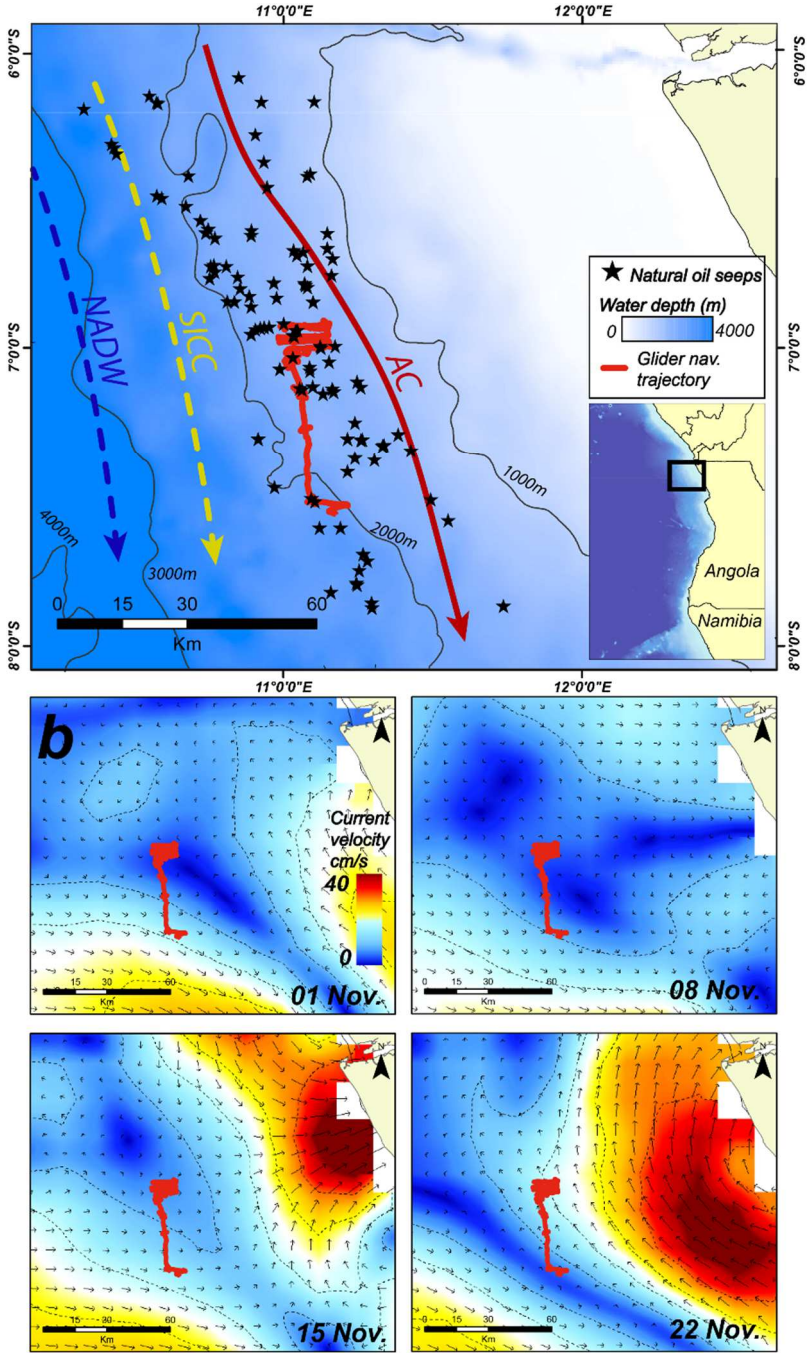

821

822 **Fig. 1: a. Map of the study area showing the location of natural oil seep sites (black stars) identified on SAR satellite images**
823 **(Jatiault et al., 2017). b. Map of weekly averaged geostrophic surface currents of the observed ocean physics (Copernicus**
824 **MULTIOBS ARMOR3D dataset; www.marine.copernicus.eu) superimposed with the glider route in red. From top left to bottom**
825 **right: 01/11, 08/11, 15/11 and 22/11/2017.**

826

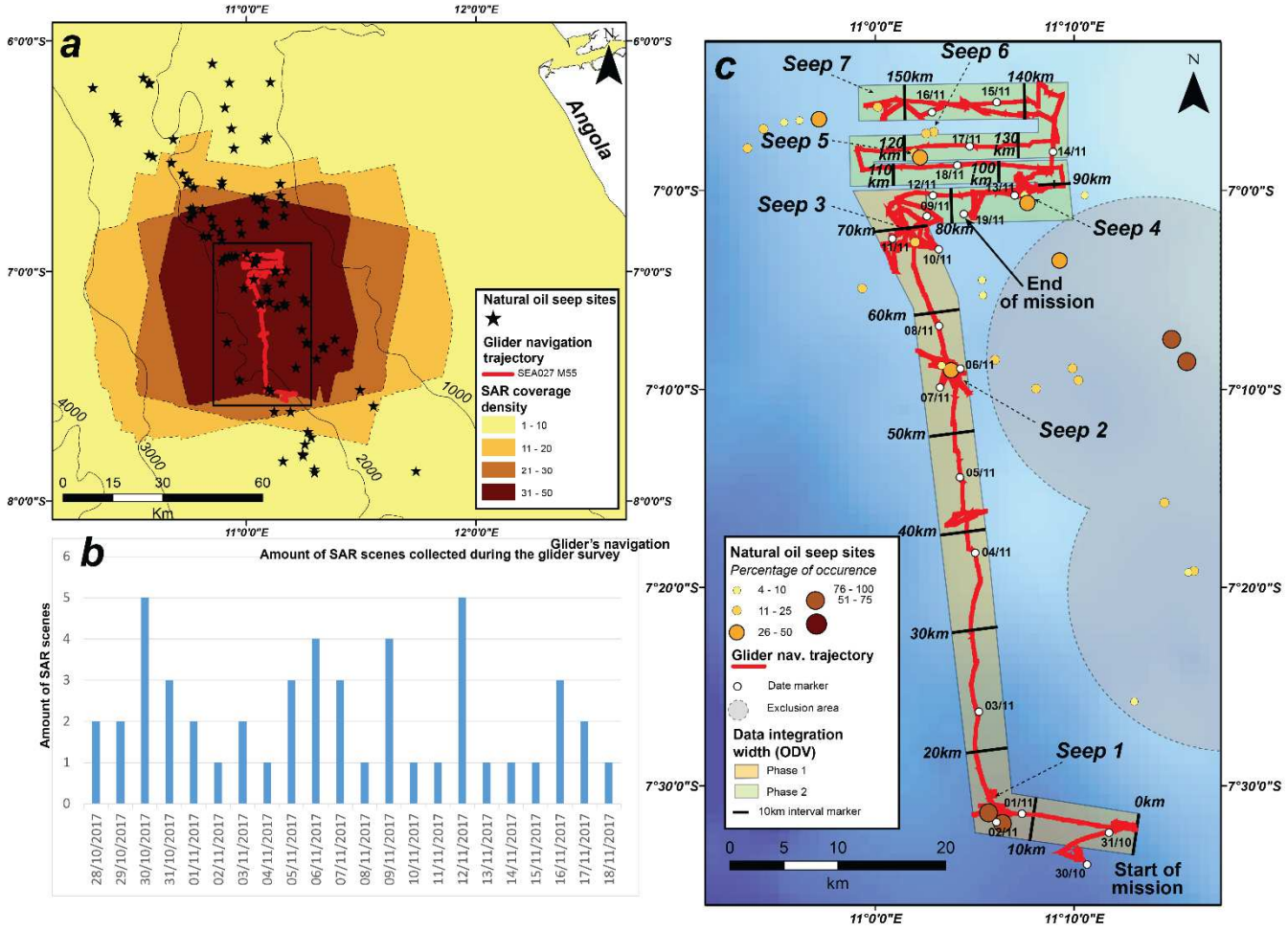

827

828 **Fig. 2: a. Density coverage of satellite scenes collected during the glider mission. Black stars correspond to the location of oil seep**
829 **sites detected during a 1994 - 2016 SAR monitoring (Jatiault et al., 2017) superimposed with the navigation trajectory of the glider.**
830 **b. Temporal distribution of SAR scenes collected during the 20 days of mission (from 29 October to 18 November 2017). c. Zoom**
831 **on the glider mission acquisition plan. White dots correspond to the temporal location of the glider. Glider data have been stacked**
832 **within a 1.5 wide strip (orange and green polygons) for the generation of 2D profiles using Ocean Data View (ODV) software.**

833

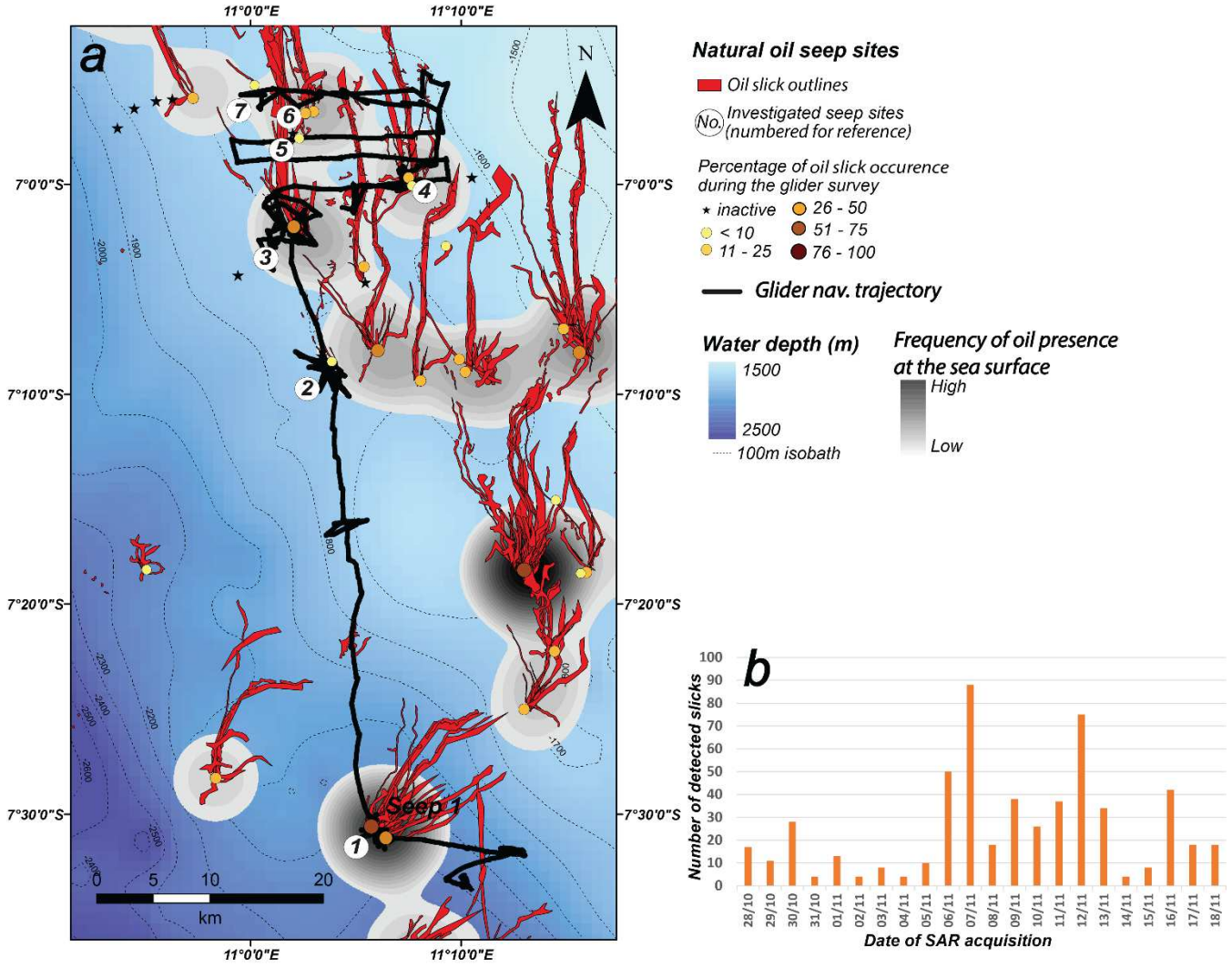

834

835 **Fig. 3: Glider trajectory (black line) superimposed with oil slicks detected on SAR images during the glider mission (20 days from**
836 **29 October 2017 to 18 November 2017). During the mission, previous oil seep sites identified between 1994 and 2016 (Jatiault et al.,**
837 **2017) were either active (coloured dots correspond to occurrence rates, i.e. the ratio between the number of slicks detected and the**
838 **SAR scene coverage density) or inactive (black stars).**

839

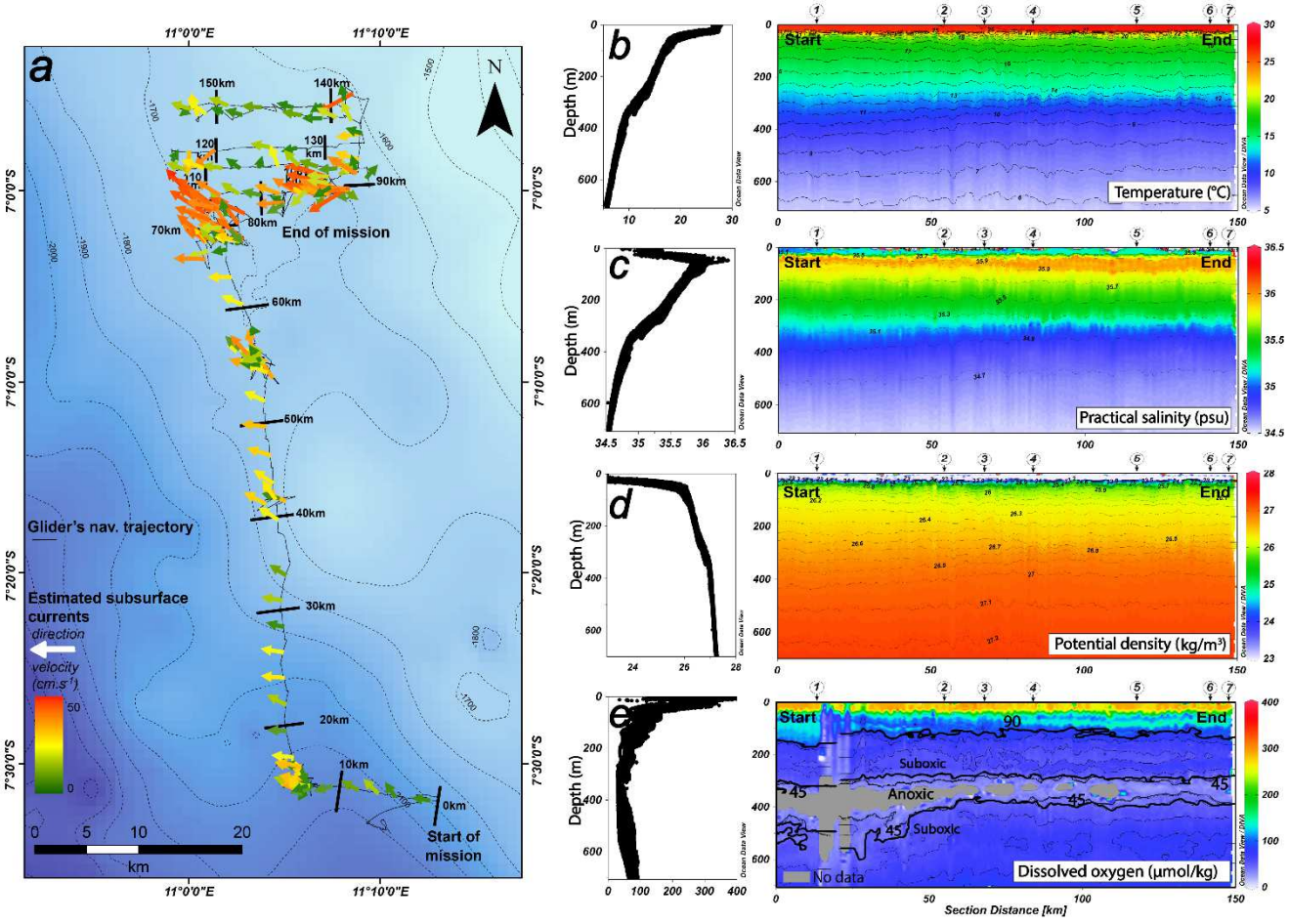

840

841 **Fig. 4: Hydrological measurements acquired with the glider. Oil seep positions are reported on top of section distance profiles. a.**
842 **Map of the estimation of underwater current (Depth Averaged Current) between the estimated and real surfacing location of the**
843 **glider. The estimated currents are superimposed with the water depth, the glider trajectory and landmarks along the glider**
844 **trajectory. b. Potential Temperature (θ). c. Practical salinity (Sp). d. Potential density (σ_θ). e. DO concentration. Each physical**
845 **parameter is displayed on a scatterplot (on the left) and on a 2D section (on the right) where measurements have been stacked**
846 **along a 1.5 km wide strip following the glider trajectory (see Fig. 2).**

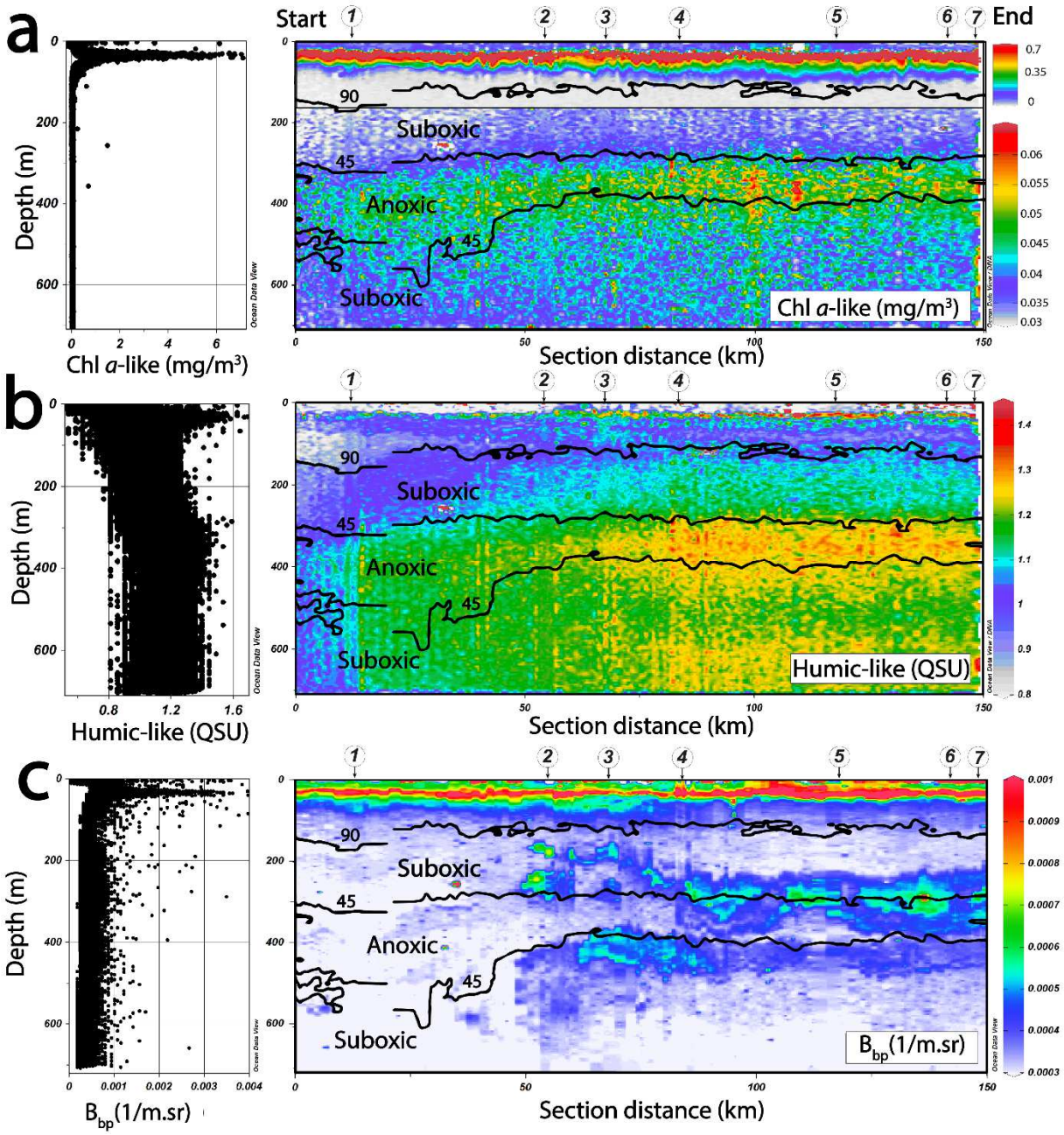

847

848 **Fig. 5: Distribution of (a) Chlorophyl-a-like concentration, (b) humic-like content and (c) the particle backscattering signal at 700**
849 **nm (bbp700). Biogeochemical parameter concentrations are superimposed with dissolved oxygen isocontours (thick black contour**
850 **lines) marking the limits between the suboxic layers and the oxygen minimum zone. Measures are displayed in scatterplots (left)**
851 **and section profiles (right).**

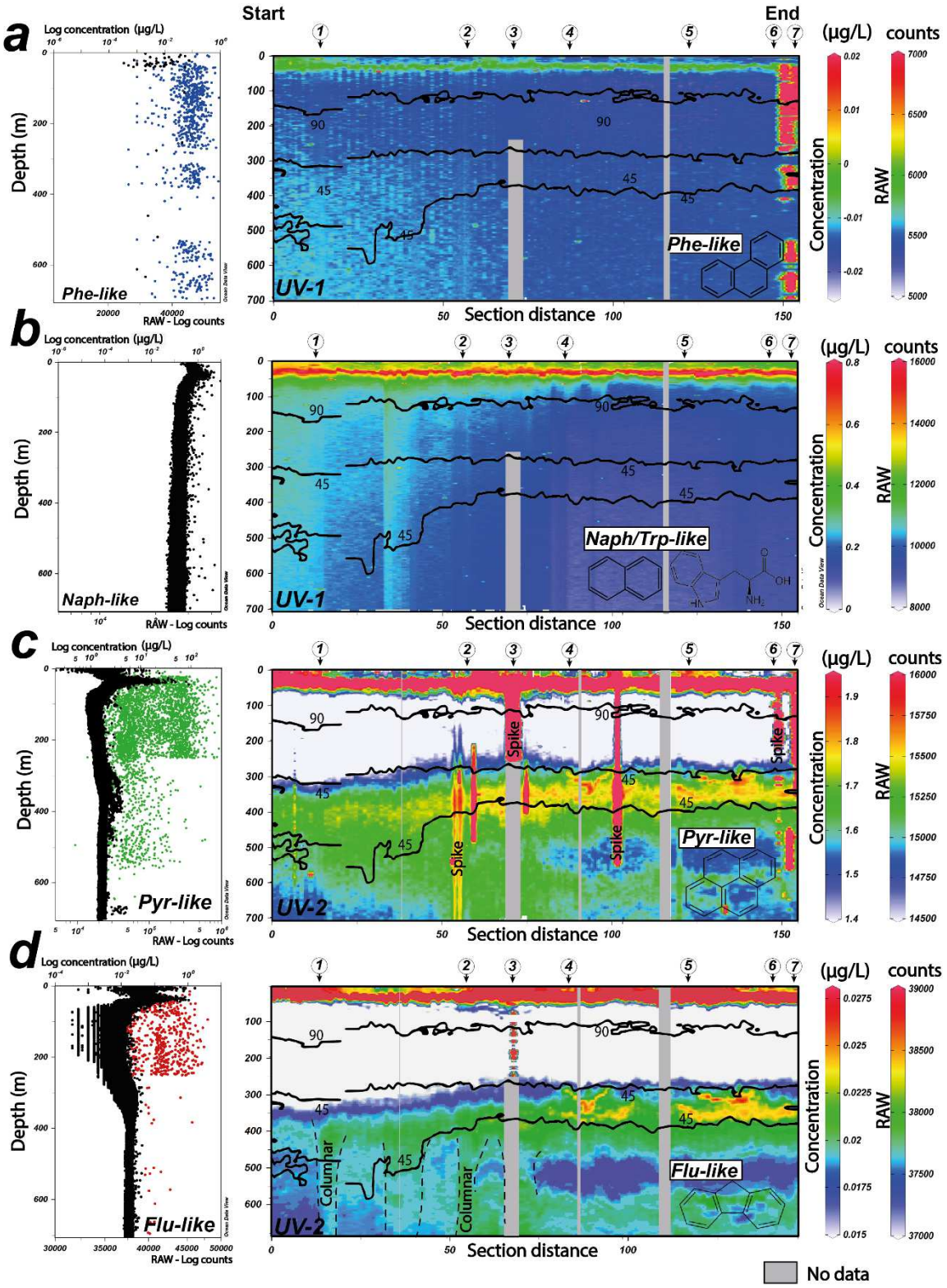
a
Log concentration (µg/L)
Depth (m)
Phe-like
RAW - Log counts
Start
End
UV-1
Phe-like
Section distance
(µg/L)
counts
Concentration
RAW
b
Naph-like
Naph/Trp-like
c
Pyr-like
Spike
UV-2
d
Flu-like
Columnar
No data

852

Fig. 6: General overview of dissolved PAH-like concentrations detected during the 20 days of acquisition by the glider. Left: PAH concentrations compared with the water depth (m) in log scale. Coloured dots correspond to spike anomalies with respect to classic profiles (black dots). Right: 2D sections displaying PAH-like measurements (raw counts and concentrations) along the glider trajectory. Colour scales were stretched in order to highlight fine-scale modification in depth compared with the prominent ~50 m anomaly. Numbers at the top of each section correspond to the location of oil seep sites identified from SAR slick analysis. Thick black contour lines correspond to DO isocontours.

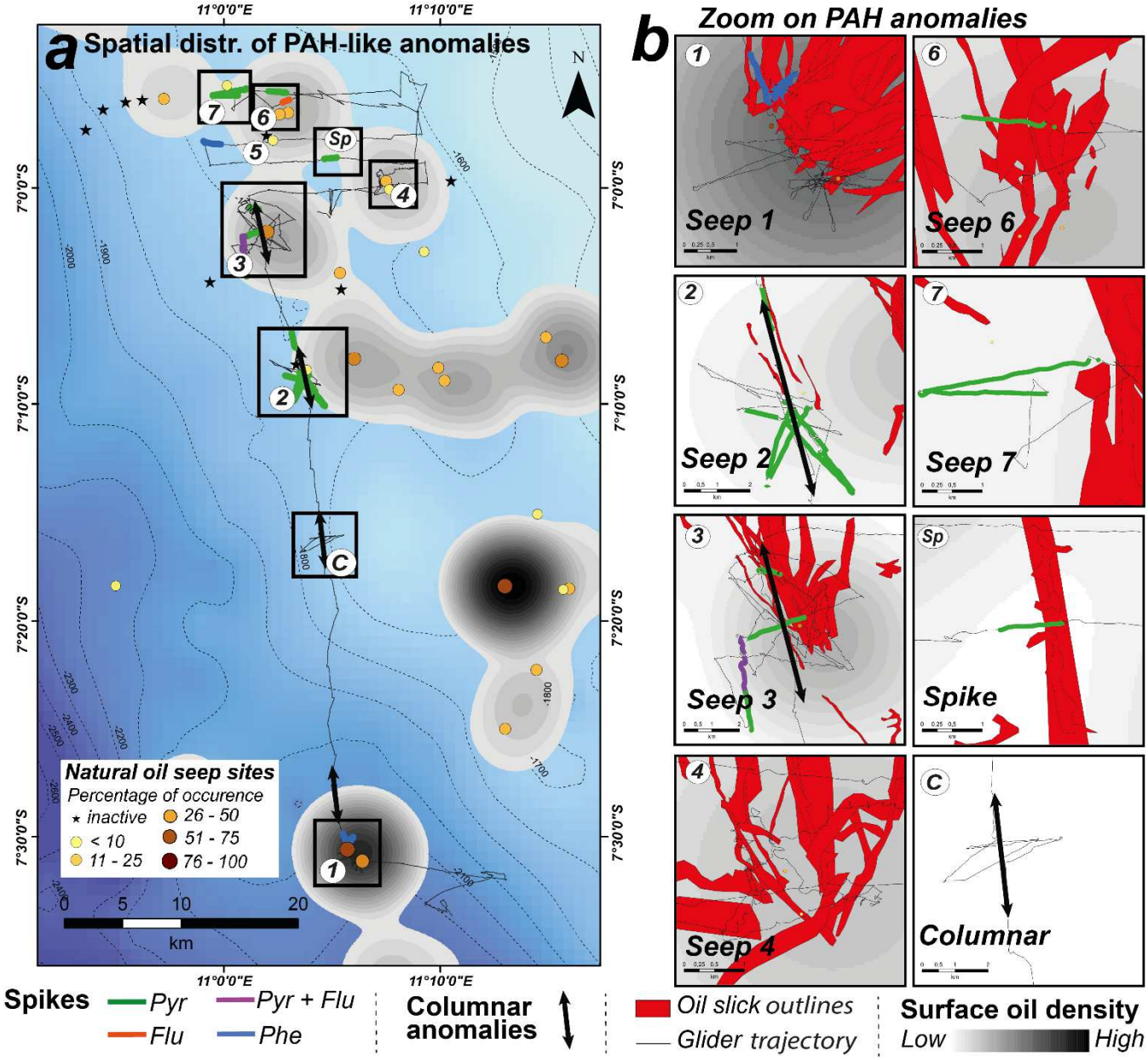

Fig. 7: a. Geographical distribution of PAH-like anomalies observed on the optical channels of the MiniFluo-UV sensors superimposed with the location of oil slick impact areas and oil seep sites. Black boxes correspond to extracts displayed in Fig. 7b. b. Zooms of PAH anomalies at frequent oil emission sites with the outlines of natural oil slicks.

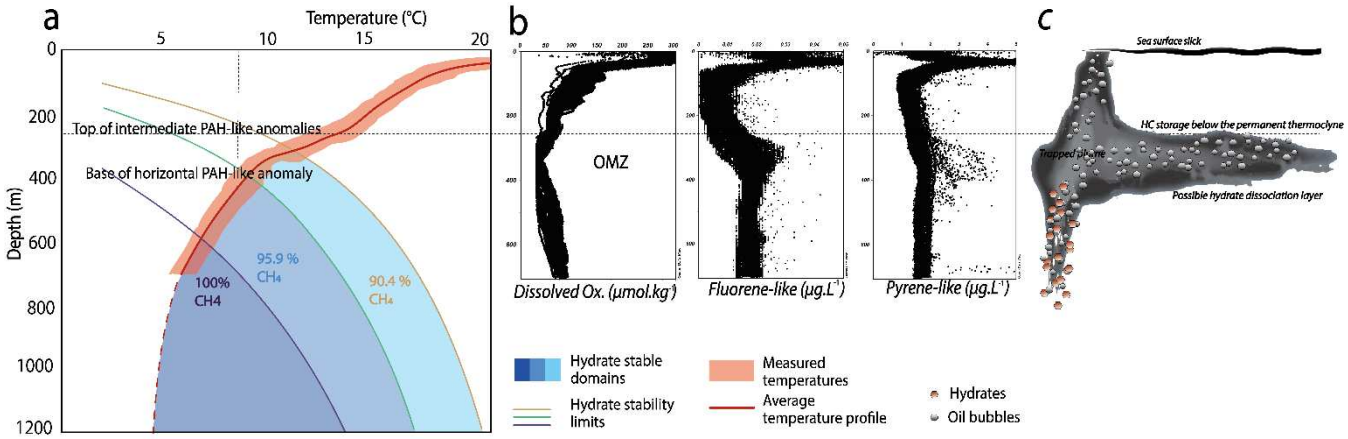

Fig. 8: a. Hydrate stability domains in the water column reported as a function of the water depth, the gas composition and in-situ temperature (Sassen et al., 1999; Milkov et al., 2000). b. Dissolved oxygen, Flu- and Pyr-like component distribution measured during the glider mission. c. Interpretative sketch of the interactions between the oil plume and physical properties of the ocean.

870 **Table 1: Main characteristics ($\lambda_{Ex}/\lambda_{Em}$ couples and limits of detection) of the different polyaromatic hydrocarbon (PAH-like) and**

871 **biochemical parameters.**

PAH-like	Excitation λ_{Ex} (nm)	Emission λ_{Em} (nm)	Limit of detection (µg L^{-1})	Sensor
Phenanthrene	255	360	0.01	MiniFluo-UV1
Naphthalene/ Tryptophan	275	340	~0.074	MiniFluo-UV1
Pyrene	270	380	0.08	MiniFluo-UV2
Fluorene	260	315	0.03	MiniFluo-UV2
Biogeochemical parameters			**Limit of detection**	
Humic-like	370	460	0.28 QSU	FLBBCD
Chlorophyll-*a*	470	695	0.015 $mg.m^{-3}$	FLBBCD
Particle backscattering b_{bp700}	700		0.0015 $m^{-1}.sr^{-1}$	FLBBCD

872

873

874